國 立 交 通 大 學

電信工程學系碩士班

碩 士 論 文

可塑性雙頻四極化掃描天線之設計

Design of the Dual-Band Reconfigurable Quadri-Polarization Diversity Antenna

研究生：邱正文 **(Cheng-Wen Chiu)**

指導教授：陳富強 博士 **(Dr. Fu-Chiarng Chen)**

中華民國九十六年九月

可塑性雙頻四極化掃描天線之設計

Design of the Dual-Band Reconfigurable Quadri-Polarization Diversity Antenna

研究生：邱正文　　**Student: Cheng-Wen Chiu**

指導教授：陳富強 博士　　**Adivsor: Dr. Fu-Chiarng Chen**

國立交通大學
電信工程學系碩士班
碩士論文

A thesis
Submitted to Department of Communication Engineering
College of Electrical and Computer Engineering
National Chiao Tung University
in Partial Fulfillment of the Requirements
for the degree of
Master
in

Communication Engineering
September 2007
Hsinchu, Taiwan, Republic of China

中華民國九十六年九月

可塑性雙頻四極化天線之設計

研究生：邱正文　　指導教授：陳富強 博士

國立交通大學電信工程系碩士班

摘要

此論文的研究方向著重於雙頻 L 形電容耦合饋入式平面天線搭配上運用奇偶模分析方式設計出的雙頻枝幹耦合器與寬頻的切換電路的設計來達成雙頻四極化的目的。此架構操作的頻率是 WiMAX (3.5GHz)與 WiFi (2.45GHz)的頻段，其中 WiMAX 更是時下熱門的應用，它相較於 WiFi 有較遠的傳輸距離、較寬的頻帶與較高的傳輸速度，這些都足以應付商業上對於傳輸資料量相對增大的多媒體資訊的需求。

極化掃描天線對於無線傳輸的優點是能透過多重極化提供更多的通訊通道增加了資料的承載量與接收端的敏感度，更較能減低多重散射環境對於訊號品質的影響。本論文也將依循著這個原則設計出能產生雙圓形與雙線性的天線架構。整體架構包含三個部分：L 形電容耦合饋入式平面天線是為了克服平面式微帶天線窄頻的缺點；雙頻枝幹耦合器提供天線在操作的兩個頻率點上各輸出兩組相差正九十度與負九十度的訊號，最後寬頻的切換電路是將枝幹耦合器的兩組訊號作分配用以激發不同方向的天線以產生線性極化模態或同時激發兩個垂直的天線以產生圓形極化模態。

Design of the Dual-Band Reconfigurable Quadri-Polarization Diversity Antenna

Student: Cheng-Wen Chiu Advisor: Dr. Fu-Chiarng Chen

Department of Communication Engineering

National Chiao Tung University

Abstract

This thesis introduces the design of a patch antenna fed by L-shaped capacitive coupling probes, along with a dual-band branch line coupler designed by the even-odd mode analysis method we proposed in this thesis and the wideband switching circuit to achieve our purpose of the dual-band quadri-polarization diversity antenna. In nowadays, WiMAX is becoming more popular in wireless communication application besides WiFi. This antenna structure operates at WiFi (2.45GHz) and WiMAX (3.5GHz) spectrum. The transmission distance, bandwidth and transmission speed of WiMAX operation are better than that of WiFi

The advantages of polarization diversity antenna include providing more channels by producing more polarization modes to enhance the capacity and receiver sensitivity and reducing the effect of multi-scattering environment. Based on these principles, we propose an antenna structure which can produce dual linear and dual circular polarizations. There are three parts in our design: first, the dual-band branch line coupler provides two equal-power signals with 90° or -90° phase difference in each operating band. Second, the wideband switching circuit controls the two output powers of branch line coupler to excite the antenna structure for producing linear polarization wave or circular polarization wave. Third, the L-shaped fed conventional planar patch antenna is provided to overcome the coupling effect.

ACKNOWLEDGEMENTS

I must offer my thanks to my family. Every time when I need them, they are always there and give me the greatest help and care. Without their support and encouragement, I could not be better than ever. Thank my professor for the free research environment he brings to us, and I learn how to find a way to solve problems and think independently. Especially, thank my fellows including Nan, Peng, Eric, LK and Y-Pen for their inspiring help and consultation.

Contents

Figure Captions

Table Captions

Chapter 1 Introduction

1.1 Motivation

Recently, the applications of WiFi (Wireless Fidelity) and WiMAX (Worldwide Interoperability for Microwave Access) are becoming more popular in wireless communication. In early stages, WiFi provide the best solution for establishing wireless local network. However in nowadays, the bandwidth and transmission speed which WiFi provides are not enough for the mass data transmission of multimedia in business application. Therefore, the specification of WiMAX which IEEE established the standard of 802.16 is set for solving these problems.

An antenna structure with various polarization modes has been applied in wireless communication. In general, the designers use two antennas in orthogonal direction and feeding two equal power signals with 90° phase difference to produce various polarizations. The polarization diversity can provide more channels to enhance the capacity and receiver sensitivity and overcome the multi-scattering environment in urban areas. Many researches have implemented these concepts to design an antenna structure with quadri-polarization states [1-2].

The most popular candidate of the antenna with various polarization modes is the rectangular patch microstrip antenna. And the techniques for feeding patches can be classified into three groups: directly coupled, electromagnetically coupled, or aperture coupled [3]. But the three conventional techniques can not offer the wide bandwidth operation of WiMAX. Recently, many researchers use the technique of L-shaped capacitive-coupled feeding method to broaden bandwidth [4].

Based on this idea, we propose an antenna structure to satisfy the dual-band requirement and solve the cross-polarization and coupling effect. The dual-band

feeding network utilizes the concept of composite right/left hand (CRLH) transmission line to provide two equal-power signals with 90° phase difference in two operation bands [5]. The method they proposed in [5] is not suitable for the dual-band branch line coupler (BLC) operate at WiFi and WiMAX applications. For solving this problem and explain this phenomena we propose another even-odd mode analysis method in this thesis to design the dual-band BLC. Moreover, we use PIN diodes to design a wideband switching circuit for controlling the output power of the dual-band BLC. By switching ON/OFF states of the PIN diodes, we can achieve the design of the dual-band quadri-polarization diversity antenna successfully.

1.2 Organization

In this thesis, we will present the dual-band quadri-polarization diversity antenna in the following chapters respectively:

Chapter 2: We will introduce the conventional planar patch antenna and polarization antenna. Furthermore, we will discuss the capacitively-coupled feeding method which will be applied in our antenna design.

Chapter 3: This chapter we propose another even-odd mode analysis method to design the dual-band BLC and a wideband switching circuit. The wideband switching circuit is composed of pin diodes and RF chokes. The pin diodes control RF power to excite the antenna or be terminated with 50-Ohm load. The RF choke provides a loop of DC bias and prevents RF power from affecting the DC power.

Chapter 4: This chapter completely introduces our antenna design with capacitively-coupled feeding technique. We will apply this technique to propose an antenna design with low coupling effect and cross-polarization.

Chapter 5: We will show the combination of these three parts we proposed previously and demonstrate the measurement results of scattering parameters and radiation patterns of the linear and circular polarization.

Chapter 6: Conclusions are drawn in this chapter.

Chapter 2 Theory of Planar Polarized Antennas

2.1 Theory of Printed Antennas

Printed antennas are popular with antenna engineers for their low profile, for the ease with which they can be configured to specialized geometries, integrated with other printed circuit and because of their low cost when produced in large quantities. Based on these advantages, microstrip patch antennas are the most common form of printed antennas and were conceived in the 1950s. Extensive investigation of patch antennas began in the 1970s [6] and resulted in many useful design configurations [7].

Figure 2-1 shows the most commonly used microstrip antenna, a rectangular patch being fed from a microstrip transmission line. The fringing fields act to extend the effective length of the patch. Thus, the length of a half-wave patch is slightly less than a half wavelength in the dielectric substrate material. An approximate value for the length of a resonant half-wavelength patch is [8]

$$L \approx 0.49\lambda_d = 0.49\frac{\lambda}{\sqrt{\varepsilon_r}} \qquad \text{Half-wavelength patch} \qquad (2\text{-}1)$$

The region between the conductors acts as a half-wavelength transmission-line cavity that is open-circuited at its ends and the electric fields associated with the standing wave mode in the dielectric. In Fig. 2-1-(c), the fringing fields at the ends are exposed to the upper half-space (Z>0) and are responsible for the radiation. The standing wave mode with a half-wavelength separation between ends leads to electric fields that are of opposite phase on the left and right halves. The x-components of the fringing fields are actually in-phase, leading to a broadside radiation pattern. This model suggests an “aperture field” analysis approach where

the patch has two radiating slot aperture with electric fields in the plane of the patch. For the half-wavelength patch case, the slots are equal in magnitude and phase. The patch radiation is linearly polarization in the xz-plane, that is, parallel to the electric fields in the slots.

Pattern computation for the rectangular patch is easily performed by first creating equivalent magnetic surface currents as shown in Fig. 2-1-(c). If we assume the thickness of the dielectric material t is small, the far-field components follow from the Equations [3]:

$$E_\theta = E_0 \cos\phi\, f(\theta,\phi) \tag{2-2a}$$

$$E_\phi = -E_0 \cos\theta \sin\phi\, f(\theta,\phi) \tag{2-2b}$$

where

$$f(\theta,\phi) = \frac{\sin\left[\frac{\beta W}{2}\sin\theta\sin\phi\right]}{\frac{\beta W}{2}\sin\theta\sin\phi}\cos\left(\frac{\beta L}{2}\sin\theta\cos\phi\right) \tag{2-2c}$$

And β is the usual free-space phase constant. The principal plane pattern follows from as

$$F_E(\theta) = \cos\left(\frac{\beta L}{2}\sin\theta\right) \qquad \text{E-plane,}\quad \phi = 0^\circ \tag{2-3a}$$

$$F_H(\theta) = \cos\frac{\sin\left(\frac{\beta W}{2}\sin\theta\right)}{\frac{\beta W}{2}\sin\theta} \qquad \text{H-plane,}\quad \phi = 90^\circ \tag{2-3b}$$

The patch width W is selected to give the proper radiation resistance at the input, often 50 Ω. An approximate expression for the input impedance of a resonant edge-fed patch is

$$Z_A = 90\frac{\varepsilon_r^2}{\varepsilon_r - 1}\left(\frac{L}{W}\right)^2 \Omega \qquad \text{Half-wavelength patch} \tag{2-4}$$

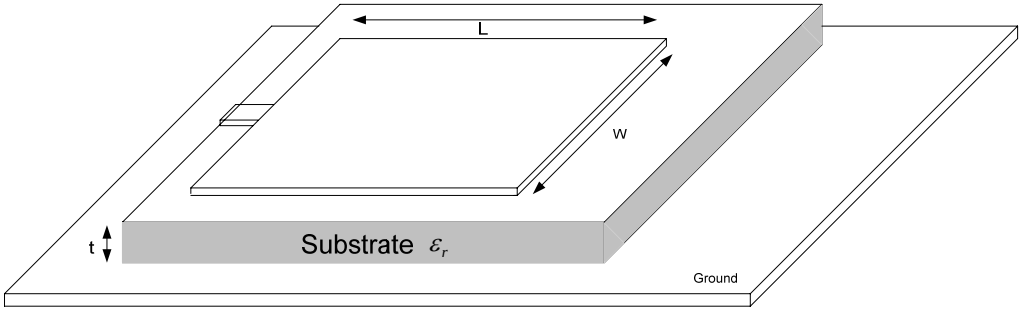

(a) Geometry for analyzing the edge-fed microstrip patch antenna

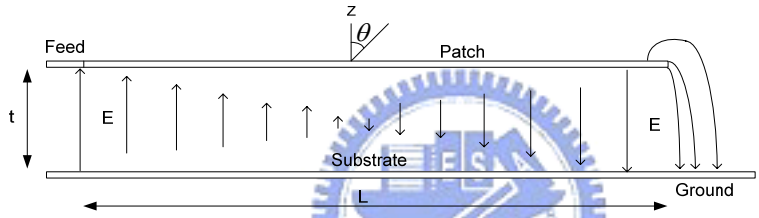

(b) Side view shown the electric fields

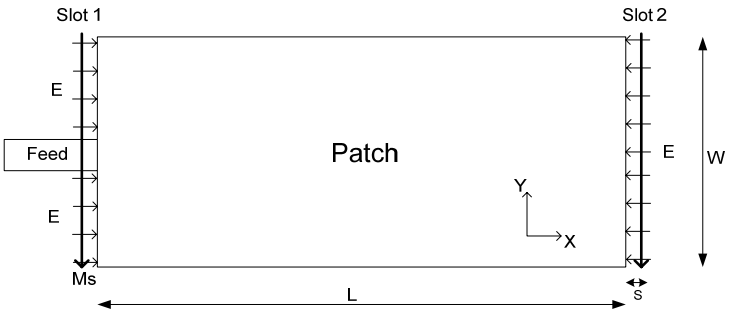

(c) Top view showing the fringing electric fields that are responsible for radiation. The equivalent magnetic surface Ms currents are also shown.

Figure 2-1 The rectangular microstrip patch antenna.

Techniques for feeding patches are summarized in Fig. 2-2. They can be classified into three groups: directly coupled, electromagnetically coupled, or aperture coupled. The direct coaxial probe feed illustrated in Fig. 2-2-(a) is simple to implement by extending the center conductor of the connector attached to the ground plane up to the patch. Impedance can be adjusted by proper placement of the probe feed. The probe feed with a gap in Fig. 2-2-(d) has the advantages of coaxial feeds. Also, the gap capacitance partially cancels the probe inductance, permitting thicker substrates.

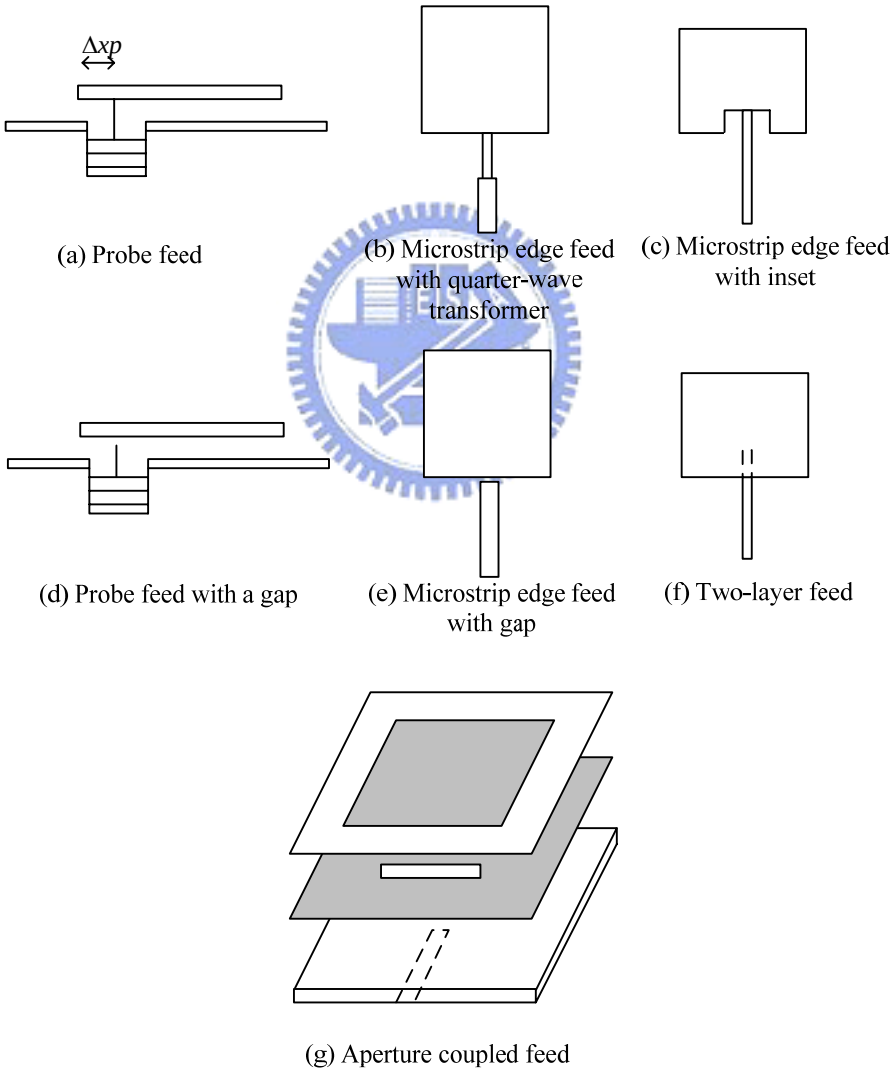

Figure 2-2 Techniques for feeding microstrip patch antennas.

Bandwidth is often ultimate limiting performance parameter and can be found from the following simple empirical formula for impedance bandwidth [9]:

$$BW = 3.77 \frac{\varepsilon_r - 1}{\varepsilon_r^2} \frac{W}{L} \frac{t}{\lambda} \quad , \quad \frac{t}{\lambda} << 1 \tag{2-5}$$

The bandwidth and efficiency of a patch are increased by increasing substrate thickness t and by lowering ε_r.

The inherently narrow impedance bandwidth is the major drawback of a microstrip patch antenna. Techniques for bandwidth enhancement have been intensively studied in past decades. Several methods including the utilization of parasitic patch [10], thick substrates [11] and capacitively-coupled feeding have been suggested in literature. The stacked geometry resulting from the addition of parasitic patches will enlarge the size and increase the complexity in array fabrication, which is especially inconvenient for the coplanar case [12].

To broaden the bandwidth in rectangular patch antenna structure, the capacitively-coupled feeding method is often chosen as the feeding topology. Recently, in Fig. 2-3, a feeding approach employing an L-shaped probe has been proposed [13]. It is already known that the L-probe has been applied successfully in other antenna designs [14]. The L-shaped probe is an excellent feed for patch antennas with a thick substrate (thickness $\approx 0.1\,\lambda_0$). The L-probe incorporated with the radiating patch introduces a capacitance suppressing some of the inductance introduced by the probe itself. With the use of a rectangular patch fed by the L–probe [15], the bandwidth and average gain can reach 35% and 7.5dBi respectively.

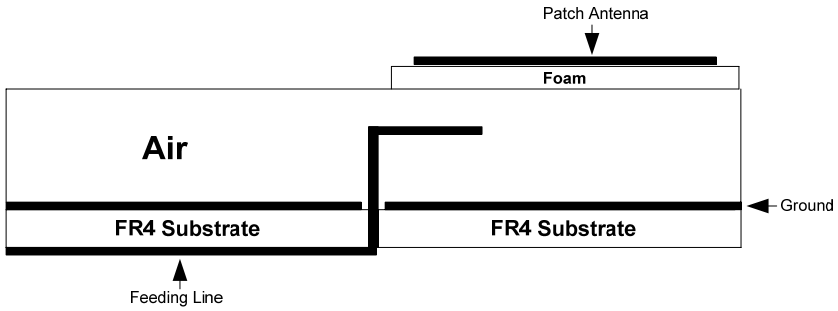

(a) Side view of L-shaped probe fed patch antenna

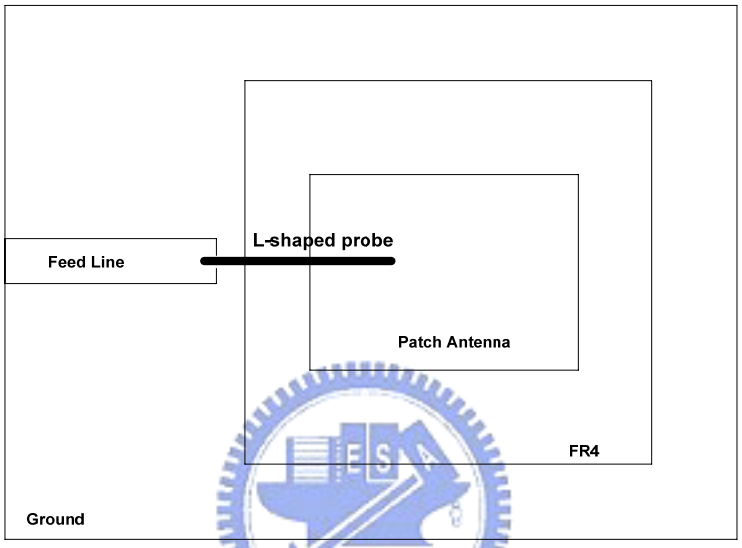

(b) Top view of L-shaped probe fed patch antenna

Figure 2-3 Patch antenna fed by L-shaped probe.

2.2 Polarization

The perspective view of a certain polarized wave shows at a fixed instant of time and the time sequence of electric field vectors as the wave passes through a fixed plane. There are some important special cases of the polarization ellipse. If the electric field vector moves back and forth along a line, it is said to be linearly polarized; as shown in Fig. 2-4a. If the electric field vector remains constant in length but rotates around in a circular path, it is circular polarized. Rotation at radian frequency ω is in one of two directions, referred to as the sense of rotation. If the wave is traveling toward the observer and the vector rotates clockwise, it is left-hand

polarized. If it rotates counterclockwise, it is right-hand polarized.

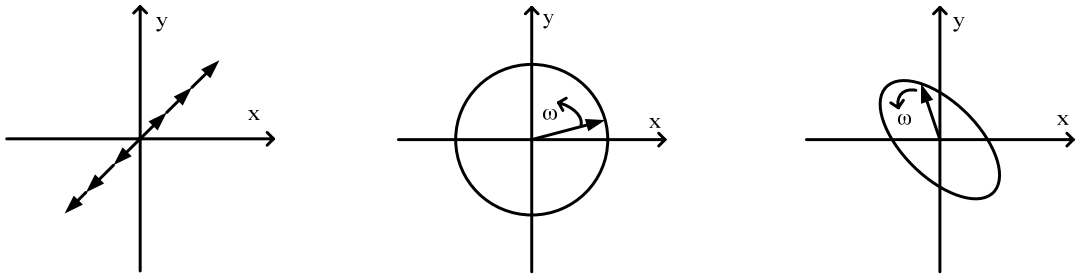

Figure 2-4 Some wave polarization states.

In Fig. 2-5a shows a left-hand circular-polarization wave, as the vector pattern translates along the +Z-axis, the electric field at a fixed point appears to rotate clockwise in the xy-plane. We can define the axial ratio (AR) as the major axis electric field component to that along the minor axis of the polarization ellipse in Fig. 2-5. The sign of AR is positive for right-hand sense and negative for left-hand sense. In Fig. 2-5, the electric field for wave can be express as:

$$\vec{E}(x,y,z,t) = (\hat{x}|E_x| + \hat{y}|E_y|e^{j\phi})e^{j(\varpi t - \beta z)} \quad (2\text{-}6)$$

In Equation (2-6), if the components are in-phase ($\varphi = 0$), the net vector is linearly polarized. If E_x=0 or E_y=0, vertical or horizontal linear polarization is produced respectively. If E_x= E_y and $\varphi = \pm 90^\circ$, the electromagnetic wave is left-hand or right-hand circular polarization with +90° or - 90° phase difference respectively, as shown in Fig. 2-5a and Fig. 2-5b.

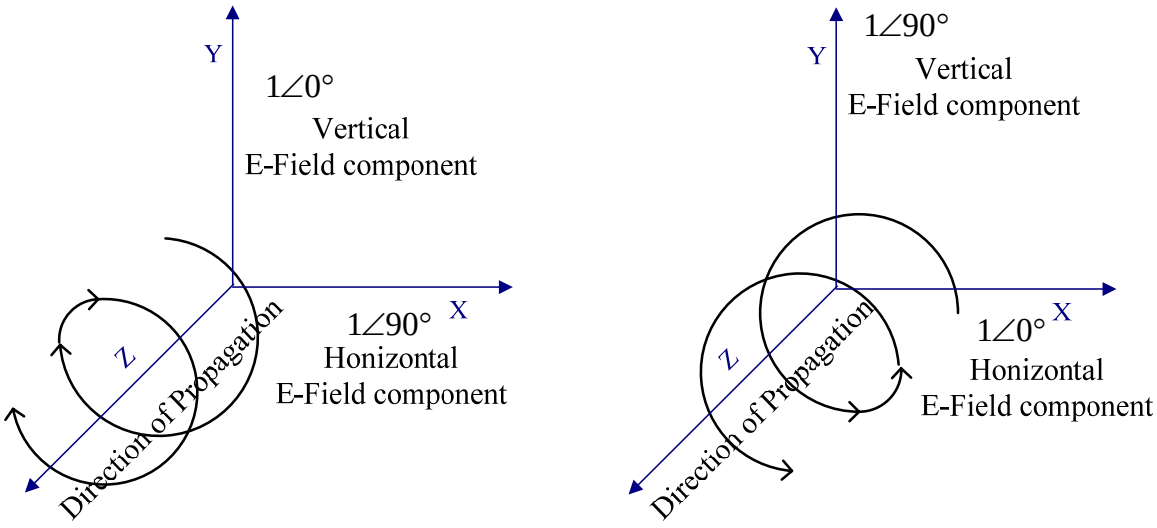

(a) Left-hand circular polarization

(b) Right-hand circular polarization

Figure 2-5 The traveling circular-polarization wave.

2.3 Polarization of an antenna

The commonly used antenna structure with certain polarization state is microstrip patch antenna. The polarization of an antenna is the polarization of the wave radiated in a given direction by the antenna when transmitting. The ideal linear- polarization antenna can be product by inverted-F antenna, microstrip patch antenna or monopole antenna. The perfect linear polarization antenna will provide linear polarization wave in one direction. When the antenna operates in linear polarization state, the cross-polarization pattern determines the performance. On the other hand, the proper circular polarization antenna is radiating two orthogonal linear polarized wave with equal power and 90° phase difference. The antenna structure with various polarization states has been discussed and applied in literature [16-17].

Chapter 3 Dual-band Branch Line Coupler with Wideband Switching Circuit

In this chapter we will propose the even-odd mode method to design the dual-band BLC and combine it with the wideband switching circuit. The dual-band BLC provides two equal power signals with 90° phase difference in two operating bands. With the wideband switching circuit, we can easily control the output power of the dual-band BLC to either go through the circuit or be absorbed by 50-Ohm termination from 2 GHz to 6 GHz.

3.1 The Theory of Dual-band BLC

The dual-band BLC can provide two signals with equal power and 90° phase difference in both operating bands, and the method of analyzing the BLC operating in two bands has been proposed in [5]. They present the composite right/left-handed (CRLH) transmission line (TL), which is the combination of an LH TL and an RH TL, to design the dual-band BLC. In Fig. 3-1, the equivalent T-model of the LH TL and RH TL exhibit phase lead and phase lag respectively. These attributes are applied to the design of a dual-band $\lambda/4$ TL. The CRLH-TL is manipulated to design electrical lengths $\pm 90^{\circ}$ at two arbitrary frequencies using this concept.

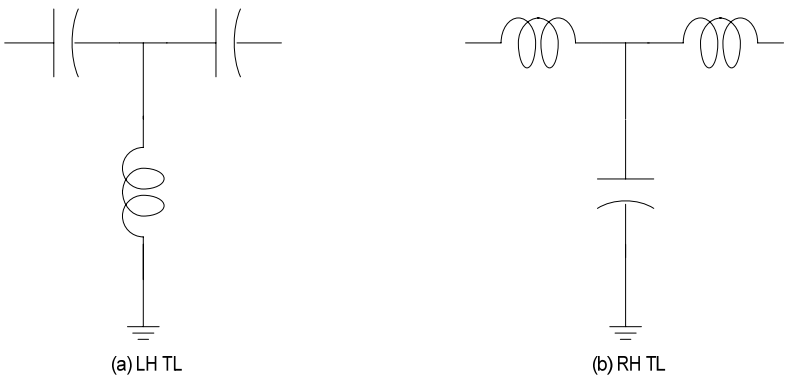

Figure 3-1 T-model of artificial RH and LH TL, respectively.

In [5], they series two (RH) right-hand TLs and LH (left-hand) two order T-model circuits to design the circuit with 90° phase shift in two operating bands respectively and through the telegrapher equations they also take $Z_{OL}=\sqrt{\frac{2\cdot L}{C}}$ into account to calculate the solution set, L (inductor) and C (capacitor) in LH T-model circuits and P_R (length of the RH TLs). The design flow of the dual-band BLC have been suggested in [5] via providing a solution set of L and C values, and P_R of the dual-band BLC at two fixed operating frequencies. Utilizing the designed flow proposed in [5] to design a BLC operated in WiFi and WiMAX applications, the solution set of C, L and P_R of the dual-band BLC we get are 1.53pF, 1.92nH, 27㎜ in the 50-Ohm branches and 2.19pF, 1.34nH, 27㎜ in the 35-Ohm branches. Then we found the solution sets we got can not operate properly in lower WiFi band. To solve the problem and explain this phenomenon, the different method of the even-odd mode analysis method is utilized in this chapter so that we can also get a solution set L, C and P_R of the dual-band BLC operated in WiFi and WiMAX applications. The even-mode and odd-mode circuits are shown in Fig. 3-2, including the circuit schematic of the equivalent type and the practical type, for solving the L and C values and P_R of the 50-Ohm branch. The odd-mode ABCD matrix of the equivalent circuit, shown in Fig. 3-2(a), can be formed by multiplying the three matrices of each cascading component and written as

$$\begin{bmatrix} A & B \\ C & D \end{bmatrix}_{odd-F_1} = \begin{bmatrix} 1 & 0 \\ -j & 1 \end{bmatrix} \begin{bmatrix} a & b \\ c & d \end{bmatrix}_{o1} \begin{bmatrix} 1 & 0 \\ -j & 1 \end{bmatrix} \tag{3-1}$$

$$\begin{bmatrix} A & B \\ C & D \end{bmatrix}_{odd-F_2} = \begin{bmatrix} 1 & 0 \\ j & 1 \end{bmatrix} \begin{bmatrix} a & b \\ c & d \end{bmatrix}_{o1} \begin{bmatrix} 1 & 0 \\ j & 1 \end{bmatrix} \tag{3-2}$$

where +90° phase difference ($\angle P_3 - \angle P_4$) is in the first band (F_1) and -90° phase difference ($\angle P_3 - \angle P_4$) is in the second band (F_2) respectively. By multiplying the three matrices of each cascading component in the practical circuit in Fig. 3-2(b), we can get

$$\begin{bmatrix} A & B \\ C & D \end{bmatrix}_{odd-F_1} = \begin{bmatrix} 1 & 0 \\ Y_{o1} & 1 \end{bmatrix} \begin{bmatrix} a & b \\ c & d \end{bmatrix}_{o1} \begin{bmatrix} 1 & 0 \\ Y_{o1} & 1 \end{bmatrix} \tag{3-3}$$

$$\begin{bmatrix} A & B \\ C & D \end{bmatrix}_{odd-F_2} = \begin{bmatrix} 1 & 0 \\ Y_{o2} & 1 \end{bmatrix} \begin{bmatrix} a & b \\ c & d \end{bmatrix}_{o2} \begin{bmatrix} 1 & 0 \\ Y_{o2} & 1 \end{bmatrix} \tag{3-4}$$

where the definition of the C in ABCD matrix is I/V and it's can be considered as the admittance of Y_o. And the Y_{o1} and Y_{o2} are obtained in F_1 and F_2 operation respectively.

$$Y_{o1} = j\frac{Z_{0R50}\omega_1 C_{50}[\omega_1^2 L_{50}C_{50} - 1] + [2\omega_1^2 L_{50}C_{50} - 1]\tan(\beta_1 P_{R50})}{2\omega_1^2 L_{50}C_{50} - 1 + Z_{OR50}\omega_1 C_{50}[1 - \omega_1^2 L_{50}C_{50}]\tan(\beta_1 P_{R50})} \tag{3-5}$$

$$Y_{o2} = j\frac{Z_{OR50}\omega_2 C_{50}[\omega_2^2 L_{50}C_{50} - 1] + [2\omega_2^2 L_{50}C_{50} - 1]\tan(\beta_2 P_{R50})}{2\omega_2^2 L_{50}C_{50} - 1 + Z_{OR50}\omega_2 C_{50}[1 - \omega_2^2 L_{50}C_{50}]\tan(\beta_2 P_{R50})} \tag{3-6}$$

And ω, C, L, P_R and Z_{OR} is the operating frequency, capacitance, inductor and the length of RH TL and characteristic of RH TL impedance respectively while the subscript 50 is the 50-Ohm branch. After comparing the formulations resulting from the equivalent circuit and the practical circuit, Equation (3-3) and (3-4) should be equal to Equation (3-1) and (3-2) and we can therefore get

$$j\frac{Z_{0R50}\omega_1 C_{50}[\omega_1^2 L_{50}C_{50} - 1] + [2\omega_1^2 L_{50}C_{50} - 1]\tan(\beta_1 P_{R50})}{2\omega_1^2 L_{50}C_{50} - 1 + Z_{0R50}\omega_1 C_{50}[1 - \omega_1^2 L_{50}C_{50}]\tan(\beta_1 P_{R50})} = -j \tag{3-7}$$

$$j\frac{Z_{0R50}\omega_2 C_{50}[\omega_2^2 L_{50}C_{50} - 1] + [2\omega_2^2 L_{50}C_{50} - 1]\tan(\beta_2 P_{R50})}{2\omega_2^2 L_{50}C_{50} - 1 + Z_{0R50}\omega_2 C_{50}[1 - \omega_2^2 L_{50}C_{50}]\tan(\beta_2 P_{R50})} = j \tag{3-8}$$

In the same manner, the even-mode ABCD matrix in the form of equivalent circuit can be written by multiplying the three matrices of each cascading component as

$$\begin{bmatrix} A & B \\ C & D \end{bmatrix}_{even-F_1} = \begin{bmatrix} 1 & 0 \\ j & 1 \end{bmatrix} \begin{bmatrix} a & b \\ c & d \end{bmatrix}_{e1} \begin{bmatrix} 1 & 0 \\ j & 1 \end{bmatrix} \tag{3-9}$$

$$\begin{bmatrix} A & B \\ C & D \end{bmatrix}_{even-F_2} = \begin{bmatrix} 1 & 0 \\ -j & 1 \end{bmatrix} \begin{bmatrix} a & b \\ c & d \end{bmatrix}_{e2} \begin{bmatrix} 1 & 0 \\ -j & 1 \end{bmatrix} \tag{3-10}$$

Similarly, the even-mode ABCD matrix in the form of the practical circuit, shown in

Fig. 3-2(b), can be written as

$$\begin{bmatrix} A & B \\ C & D \end{bmatrix}_{even-F_1} = \begin{bmatrix} 1 & 0 \\ Y_{e1} & 1 \end{bmatrix} \begin{bmatrix} a & b \\ c & d \end{bmatrix}_{e1} \begin{bmatrix} 1 & 0 \\ Y_{e1} & 1 \end{bmatrix} \tag{3-11}$$

$$\begin{bmatrix} A & B \\ C & D \end{bmatrix}_{even-F_2} = \begin{bmatrix} 1 & 0 \\ Y_{e2} & 1 \end{bmatrix} \begin{bmatrix} a & b \\ c & d \end{bmatrix}_{e2} \begin{bmatrix} 1 & 0 \\ Y_{e2} & 1 \end{bmatrix} \tag{3-12}$$

where

$$Y_{e1} = j\frac{-Z_{0R50}\omega_1 C_{50} + \omega_1{}^2 L_{50}C_{50}\tan(\beta_1 P_{R50}) - \tan(\beta_1 P_{R50})}{\omega_1{}^2 L_{50}C_{50} - 1 + Z_{0R50}\omega_1 C_{50}\tan(\beta_1 P_{R50})} \tag{3-13}$$

$$Y_{e2} = j\frac{-Z_{0R50}\omega_2 C_{50} + \omega_2^2 L_{50}C_{50}\tan(\beta_2 P_{R50}) - \tan(\beta_2 P_{R50})}{\omega_2^2 L_{50}C_{50} - 1 + Z_{0R50}\omega_2 C_{50}\tan(\beta_2 P_{R50})} \tag{3-14}$$

and the Y_{e1} and Y_{e2} is obtained in F_1 and F_2 operation respectively. We can therefore get another two equations from Equation (3-9) to Equation (3-14) as

$$j\frac{-Z_{0R50}\omega_1 C_{50} + \omega_1{}^2 L_{50}C_{50}\tan(\beta_1 P_{R50}) - \tan(\beta_1 P_{R50})}{\omega_1{}^2 L_{50}C_{50} - 1 + Z_{0R50}\omega_1 C_{50}\tan(\beta_1 P_{R50})} = j \tag{3-15}$$

$$j\frac{-Z_{0R50}\omega_2 C_{50} + \omega_2^2 L_{50}C_{50}\tan(\beta_2 P_{R50}) - \tan(\beta_2 P_{R50})}{\omega_2^2 L_{50}C_{50} - 1 + Z_{0R50}\omega_2 C_{50}\tan(\beta_2 P_{R50})} = -j \tag{3-16}$$

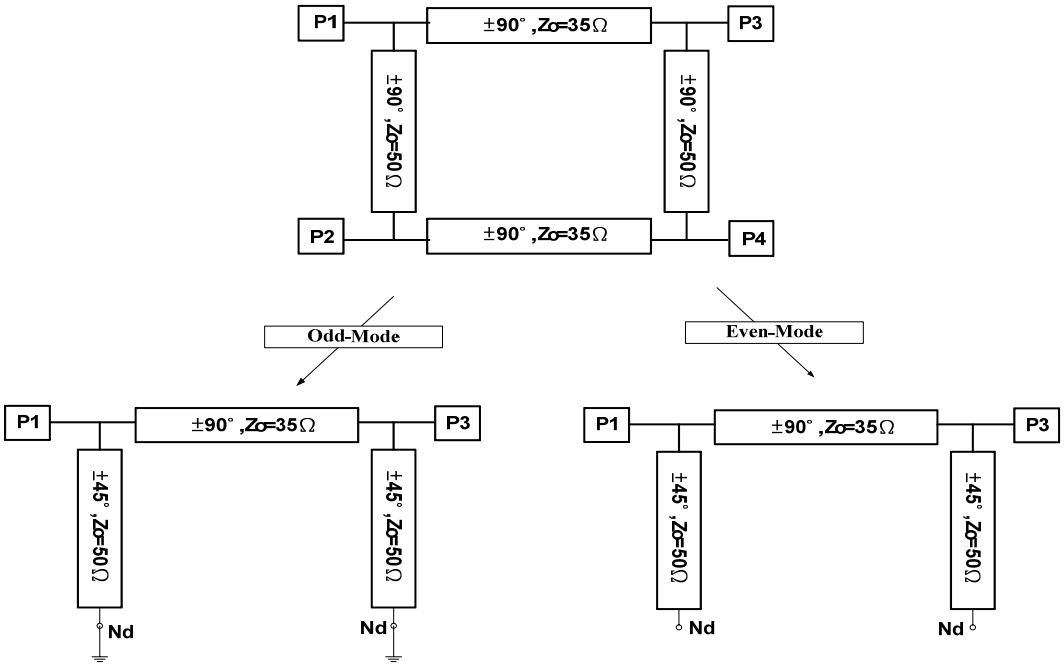

(a)

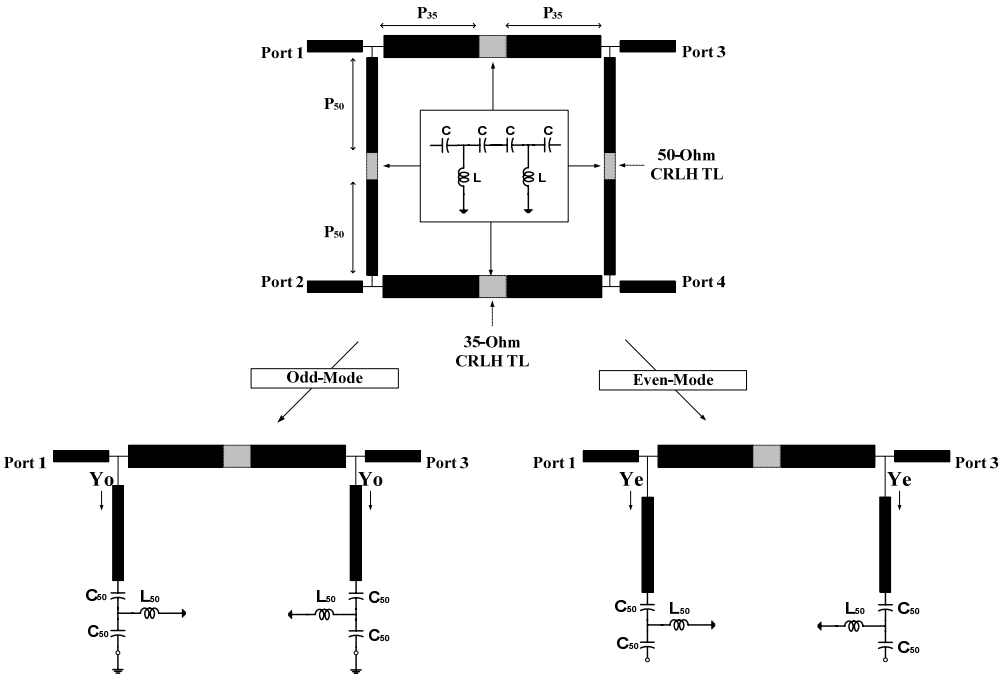

(b)

Figure 3-2 The even-mode and odd-mode circuit. (a) Equivalent circuit. (b) Practical circuit.

Directly solving exact values of the three variables (C_{50}, L_{50} and P_{L50}) from Equation (3-7), (3-8), (3-15) and (3-16) the solution set of C_{50}, L_{50} and P_{L50} of the dual-band BLC we get are 1.59pF, 2.64nH and 24.7㎜ in the 50-Ohm branches. The same analysis sequence can be applied to find the solution set of C_{35}, L_{35} and P_{L35} and we got 2.28pF, 1.85nH and 24.7㎜ in 35-Ohm branches. To exactly describe the properties of the T-model circuit, the ABCD matrix of the T-model circuit must equal to the ABCD matrix of the transmission line with phase shift θ_L and characteristic impedance Z_{OT}, so that we can got

$$Z_{OT} = \sqrt{\frac{2L}{C} - \frac{1}{\omega^2 C^2}} \tag{3-17}$$

$$\theta_L = \arctan\left(\frac{\sqrt{2\cdot\omega^2 LC - 1}}{1-\omega^2 LC}\right) \tag{3-18}$$

In equation (3-17), the Z_{OT} is depend on operating frequency and the $\frac{1}{\omega^2 C^2}$ term can be neglected in high frequency and the value of Z_{OT} affected by the $\frac{1}{\omega^2 C^2}$ term

seriously in low frequency. Thus the $Z_{OL} = \sqrt{\frac{2 \cdot L}{C}}$ derived by telegrapher equation in [5] can describe the circuit in high frequency but not in low frequency.

In Fig. 3-3, a testing circuit schematic is setting to observe the properties of the two order T-model circuits solved by the method proposed in [5] and the even-odd mode method proposed in this chapter individually and verify the circuits designed by two different analysis methods can absolutely work or not. In Fig. 3-3, one of the ports of the two-order T-model circuits is connects to a termination Z_{OR} and we observe the return loss at the other port of the testing circuit. In Fig. 3-4, the S_{T1} curve is referring to the return loss of the testing circuit in which the L_{50} and C_{50} are obtained by the design flow proposed in [5] and S_{T2} curve is referring to the return loss of the testing circuit in which the L_{50} and C_{50} are solved by our even-odd mode analysis method. At 2.45GHz, the S_{T1} is about -6.7dB which is larger than -10dB and the S_{T2} is about -74dB. The smaller the dB value of the return loss is, the two order T-model circuits can further considered as a transmission line with phase shift θ_L and characteristic impedance Z_{OT} (Z_{OT} is very close to Z_{OR} in two operating frequencies). So the solution set of the L, C and P_R in the dual-band hybrid solved by the designed flow proposed in [5] can not work well in lower WiFi band. By increasing the order of the T-model circuit to three the return loss of the T-model circuit designed by the method proposed in [5] can be small than -10dB at 2.45GHz, as shown in Fig. 3-4 S_{T3} curve, but we can just use the two order T-model circuits to achieve the same goal. Because the L and C value of the lump-elements are slightly various with frequency, we make some adjustment to let the dual-band BLC work properly at WiFi and WiMAX operations. The practical C, L and P_R of the dual-band BLC are 1.5 pF, 1.6 nH and 21.55 mm in the 35-Ohm branches, and 1.2 pF, 1.8 nH and 21.55 mm in the 50-Ohm branches, as shown in Table 3-1. Consequently, through our

even-odd mode method to design the dual-band BLC with two order T-model circuits, the dual-band BLC can properly work at both operating band as shown in next section 3.3.

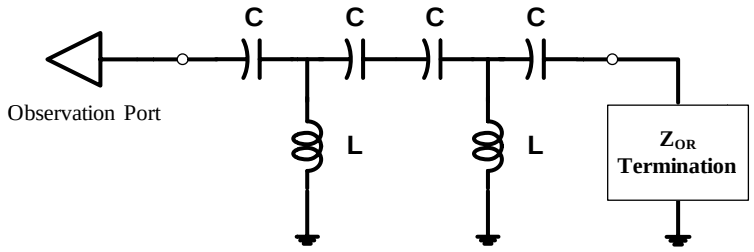

Figure 3-3 The testing circuit schematic.

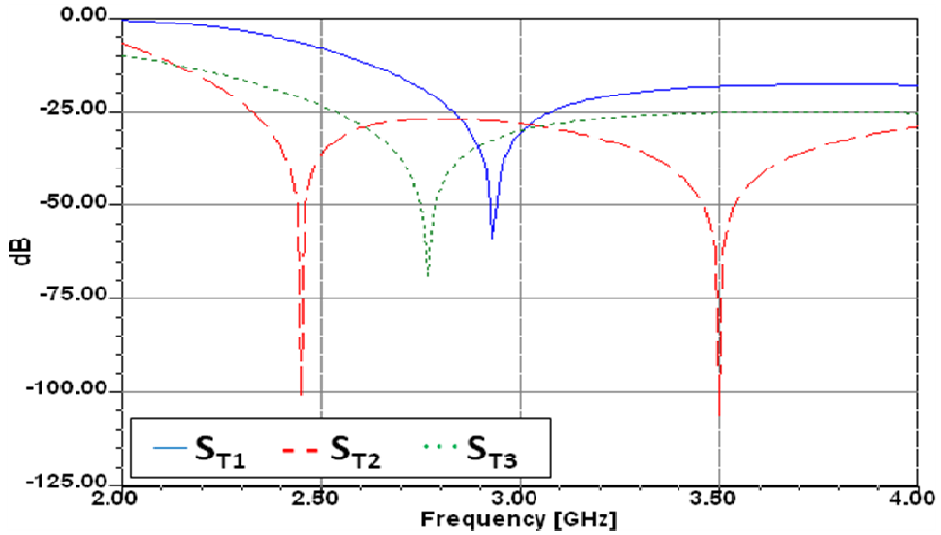

Figure 3-4 The simulated return loss of the testing circuits.

Table 3-1 The DIMENSION AND LC VALUES WE IMPLEMENT IN THE DUAL-BAND BLC.

	Zo = 35ohm	Zo = 50ohm
P (mm)	21.5	21.5
C(pF)	1.5	1.2
L(nH)	1.6	1.8

3.2 Design of Wideband Switching Circuit

An RF choke circuit is usually implemented in order to block the RF signals and make the circuit operation correctly. The conventional circuit of RF choke is shown in Fig. 3-5a. If the power is incident into RF port 1, because the quarter-wavelength TL is a narrow-band element operating in single band, and can be considered a very high inductive impedance, the power will not travel to DC port and be received at RF port 2. However, the inductor must be kept in the high impedance state in the dual-bands we desire to block the RF signal and provide a path for DC bias. As a result, the circuit of wideband RF choke is sketched as a solution in Fig. 3-5b. As shown in Fig. 3-5b, the power is incident from the RF port1, and there is only little leaky power traveling to DC port because of the high inductive impedance Ls. Most power will therefore travel to RF port 2. Based on this concept, we design a wideband switching circuit as shown in Fig. 3-6. By changing the state of pin diodes, we can control the power travels to either RF2 port or 50Ω termination. As the D1 is at “ON” state, D2 is at “OFF” state and the power incident from RF1, the power cannot travel to RF2. As the D1 is at “OFF” state, D2 is at “ON” state and the power incident from RF1, most of the power will travel to RF2. The final chosen values of capacitor, inductor and resistor are 66nH, 30pF and 50Ω, respectively.

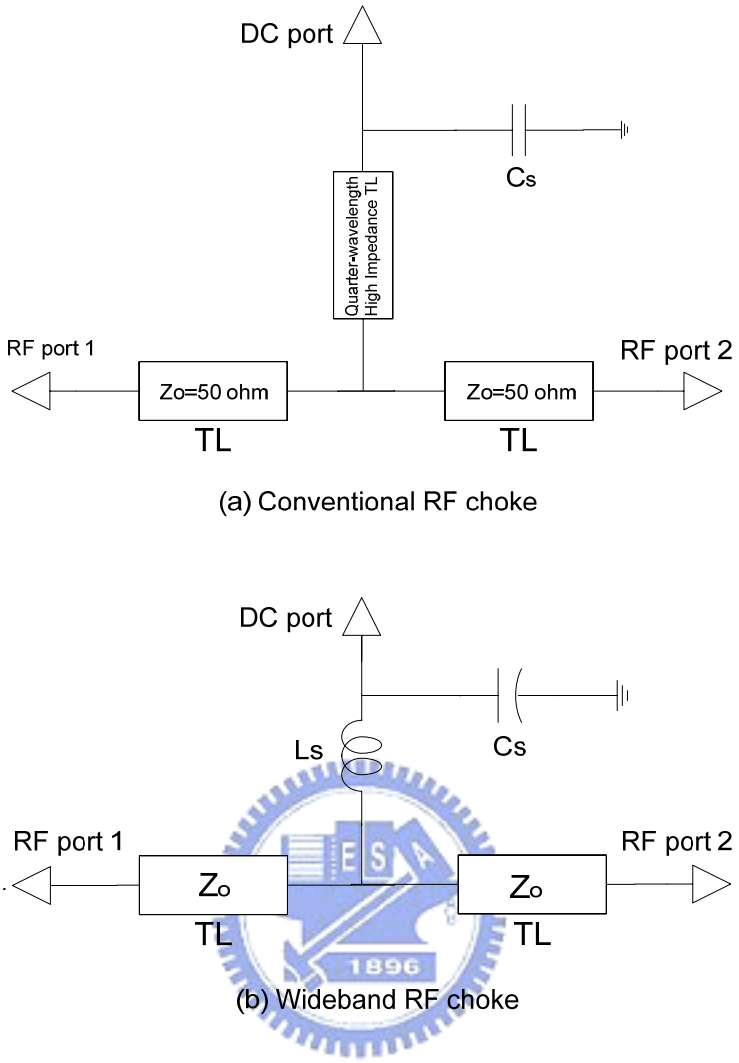

Figure 3-5 The schematic circuit of RF choke.

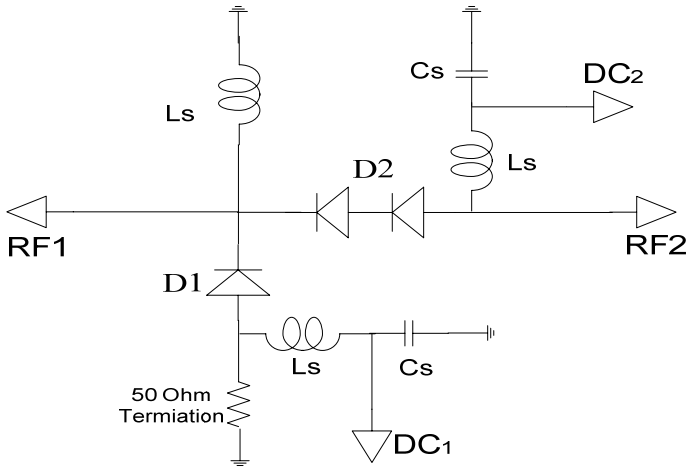

Figure 3-6 The schematic circuit of wideband switch.

3.3 Simulation and Measurement Results

In this section, we will combine the dual-band BLC and the wideband switching circuit. The circuit schematic of the combination circuit is shown in Fig. 3-7. As the power is incident from Port1 and wideband switching circuit (1) and circuit (2) in Fig. 3-7 is at “Through” state and “Termination” state, only Port2 have output power. As the power is incident from Port1 and wideband switching circuit (1) and circuit (2) are at “Through” state, the power at Port2 and Port3 is equal and the phase difference between two ports is 90°. In Table 3-2, we list four operating senses resulting from the combination of the dual-band BLC and wideband switching circuit.

We utilized HFSS to simulate the dual-band BLC and the simulated performances of Case 2 and Case 4 in Table 3-2 are shown In Fig. 3-8 and Fig. 3-9. From Fig 3-8 and Fig 3-9, the power difference between two output ports of the BLC is 0.47 dB and 0.52 dB respectively in the center frequency of WiFi and WiMAX operation in Case 2 state. Moreover, the simulated angle difference between two output ports is 84 deg and -86 deg in center frequency of WiFi and WiMAX operation in Case 2 state, respectively as shown in Fig.3-10.

The measured performances of Case 2 and Case 4 in Table 3-2 are shown In Fig. 3-11 and Fig. 3-12. In Fig. 3-11 and Fig. 3-12, we find the bandwidth and the two equal-power branches with 90° phase difference of this circuit are good for WiFi and WiMAX applications. From Fig 3-11 and Fig 3-12, the power difference between two output ports of the BLC is 0.69 dB and 0.77 dB respectively in the center frequency of WiFi and WiMAX operation in Case 2 state. Moreover, the measured angle difference between two output ports is 83 deg and -98 deg in center frequency of WiFi and WiMAX operation in Case 2 state, respectively as shown in Fig. 3-13. Because of the value deviation of lumped elements and the soldering effect, the experimental

results are slightly different from the simulation results. Fortunately, the measured bandwidth in each operating band is about 200MHz, so it is still feasible for covering each of the required bandwidth. From Fig. 3-8 to Fig. 13, the two output power in WiMAX operation are lower than the two output power in WiFi operation. It's caused by the wavelength in WiMAX operation is shorter than the wavelength in WiFi operation, so the discontinuity area is increased and may affect the performance in WiMAX operation.

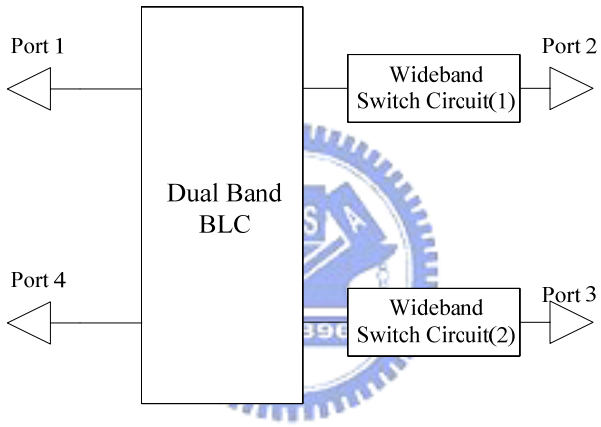

Figure 3-7 Combination of the dual-band BLC and two wideband switching circuits.

Table 3-2 THE OPERATING SENSE OF FOUR STATES OF COMBINATION OF THE DUAL-BAND BLC AND TWO WIDEBAND SWITHCING CIRCUITS.

	Intput	Switching circuit (1)	Switching circuit (2)	Output
Case 1	**Port 1**	**Through**	**Termination**	**Port2**
Case 2	**Port 1**	**Through**	**Through**	**Port2 and Port3**
Case 3	**Port 4**	**Termination**	**Through**	**Port3**
Case 4	**Port 4**	**Through**	**Through**	**Port2 and Port3**

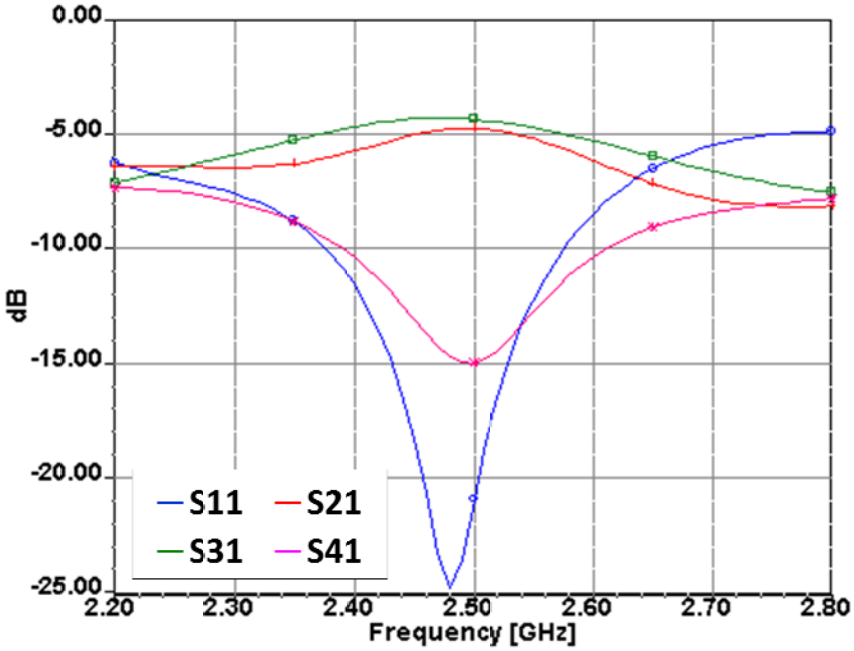

(a) WiFi operation.

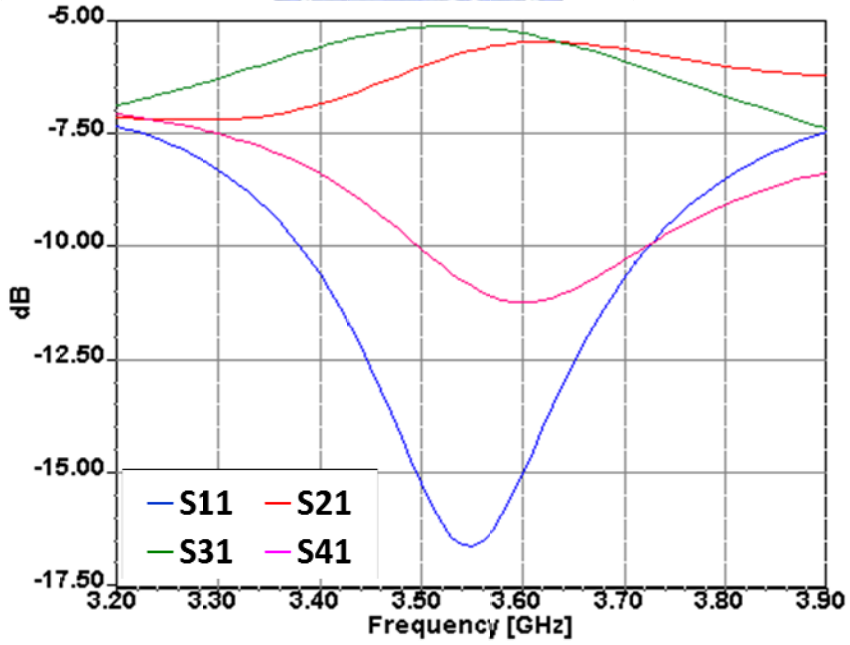

(b) WiMAX operation.

Figure 3-8 The simulated results of the dual-band BLC in Case 2 state.

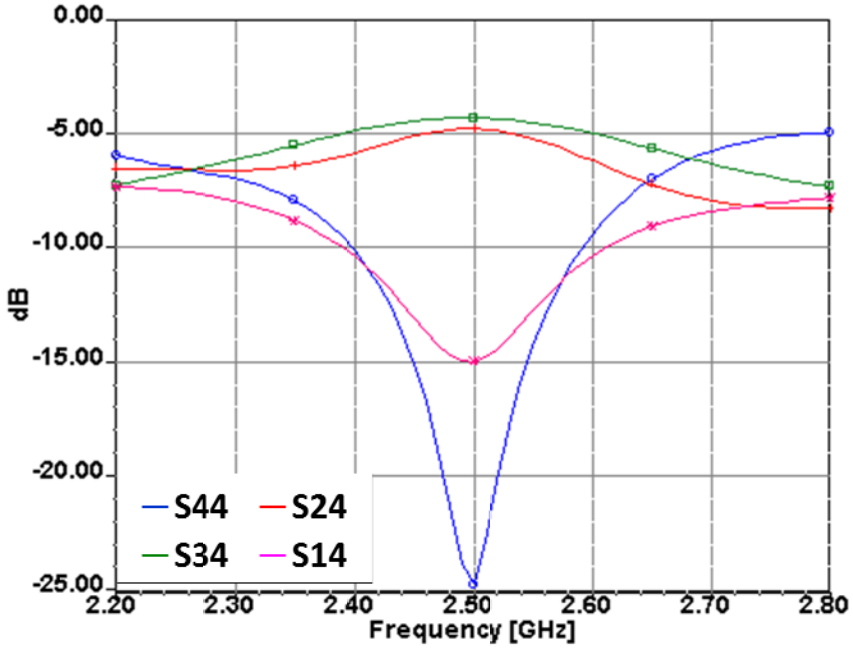

(a) WiFi operation.

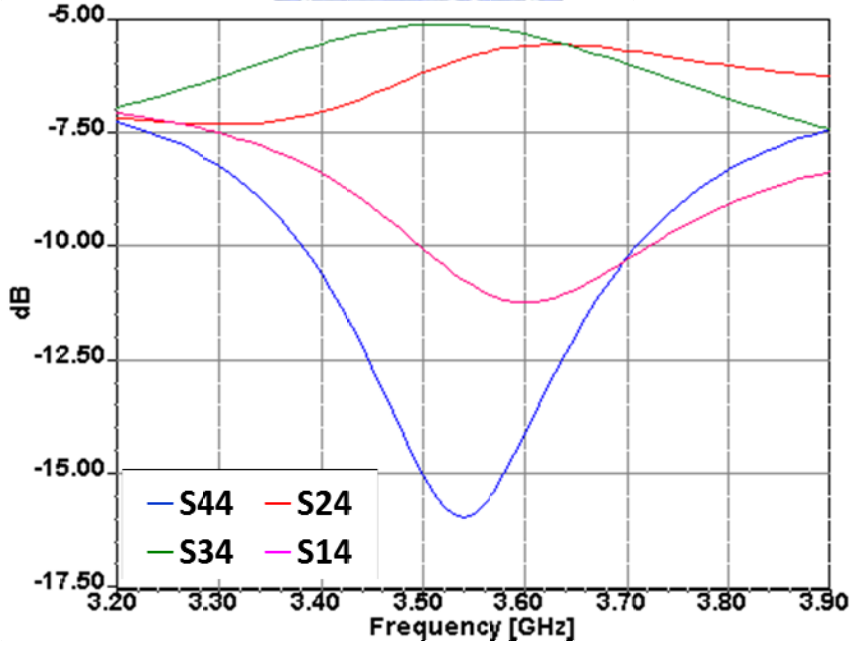

(b) WiMAX operation.

Figure 3-9 The simulated results of dual band BLC in Case 4 state.

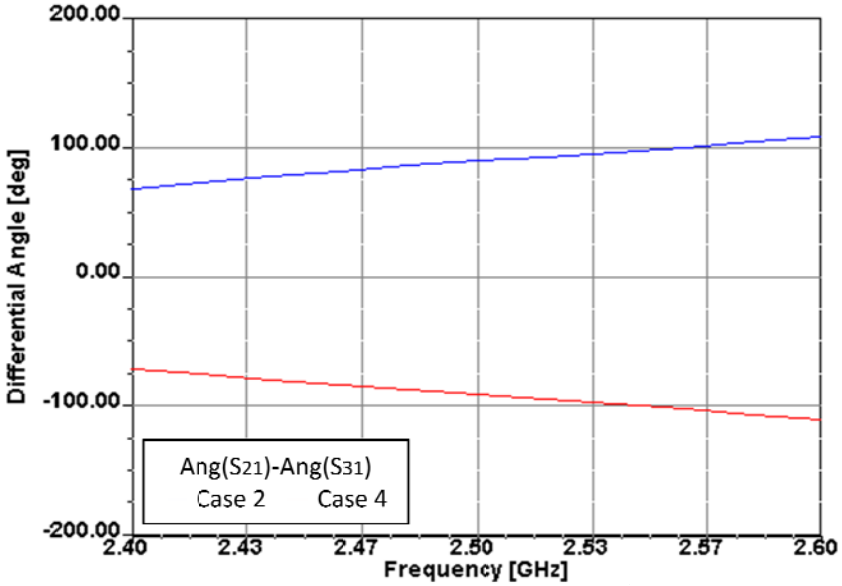

(a) WiFi operation.

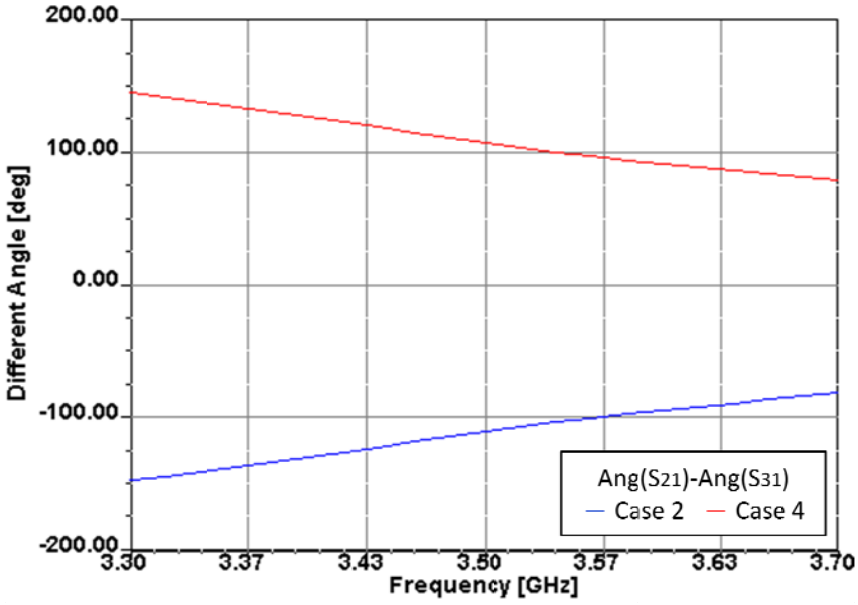

(b) WiMAX operation.

Figure 3-10 The simulated angle difference of the dual-band BLC.

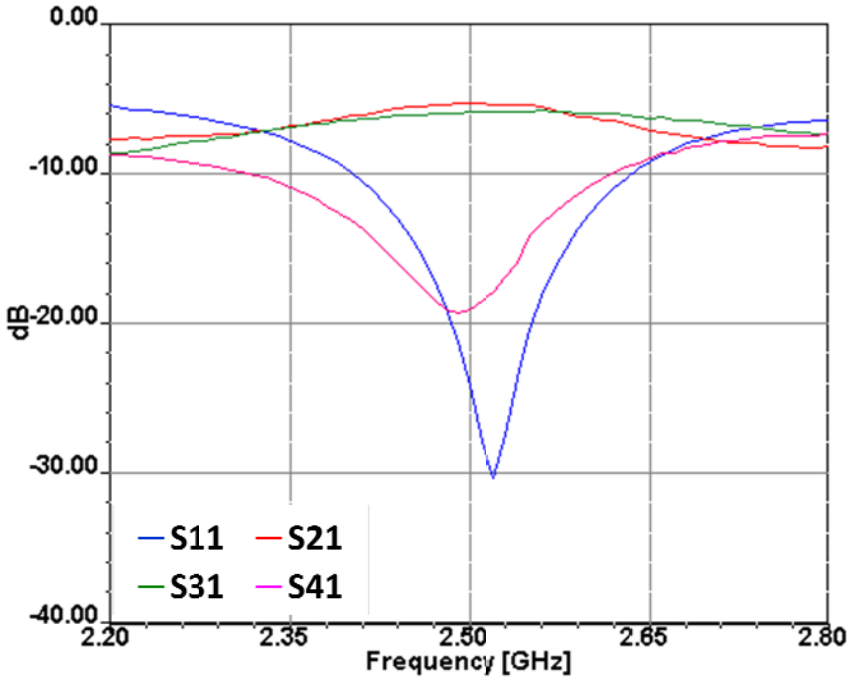

(a) WiFi operation.

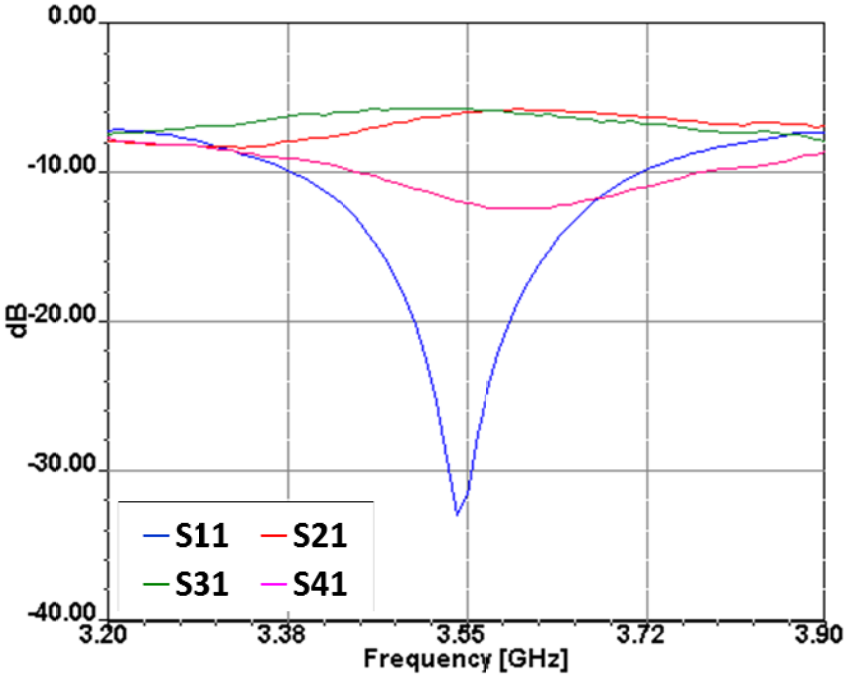

(b) WiMAX operation.

Figure 3-11 Measured scattering parameters of combination of the dual-band BLC with two wideband switching circuits in Case 2 state.

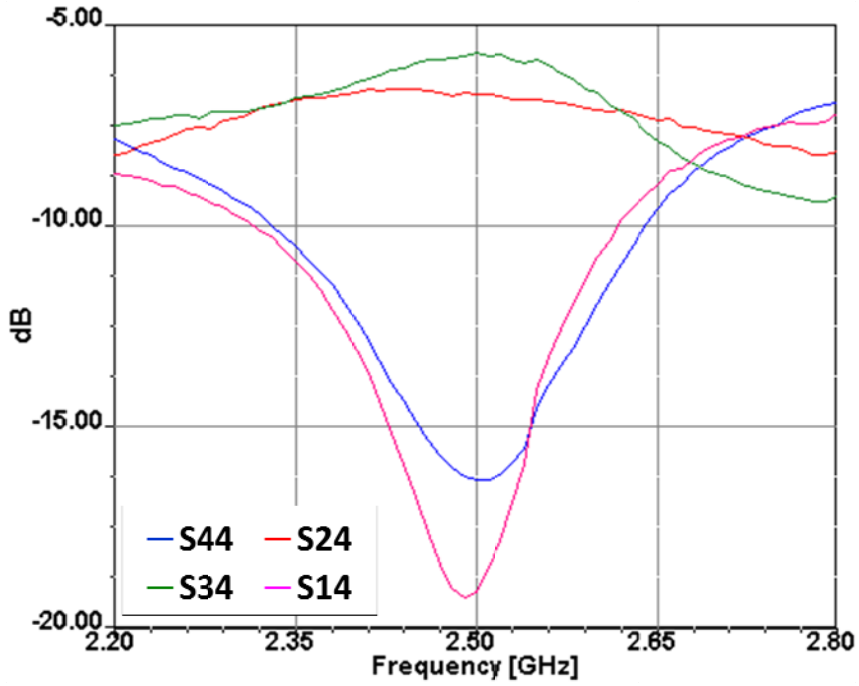

(a) WiFi operation.

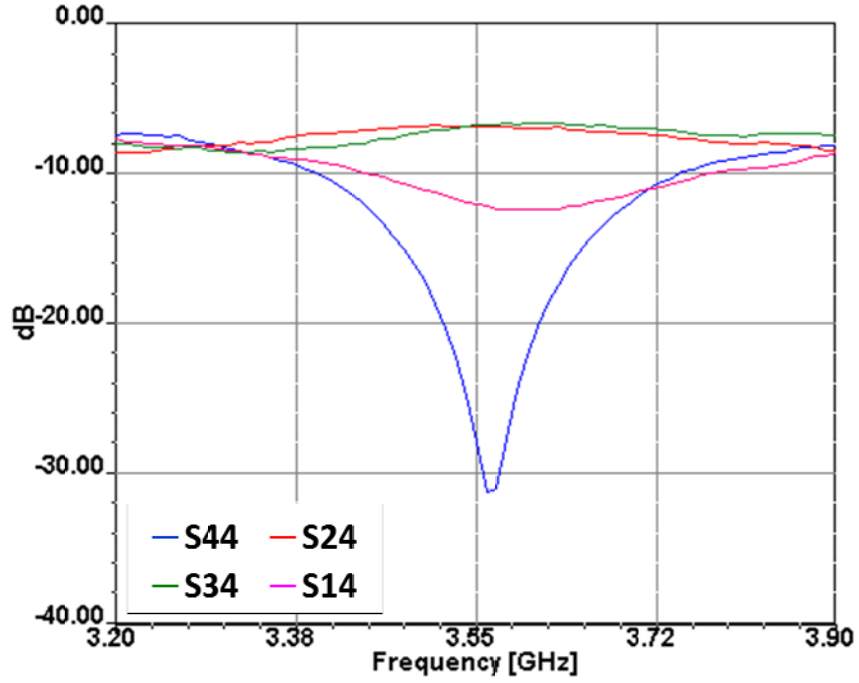

(b) WiMAX operation.

Figure 3-12 Measured scattering parameters of combination of the dual-band BLC with two wideband switching circuits in Case 4 state.

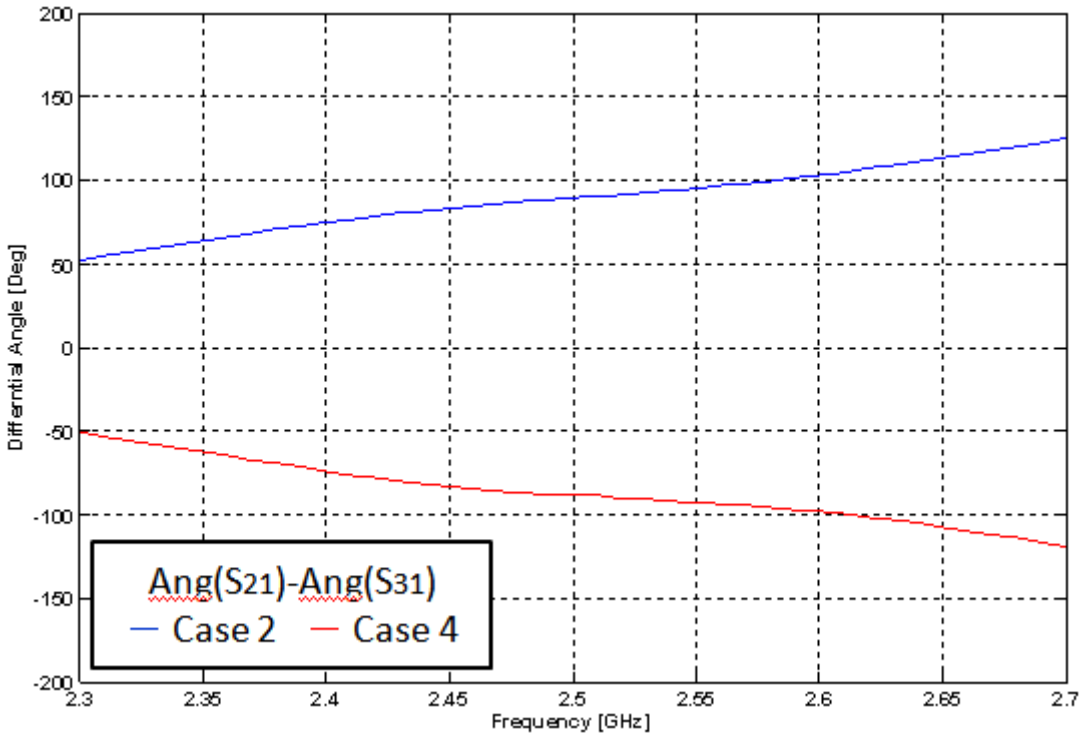

(a) WiFi operation

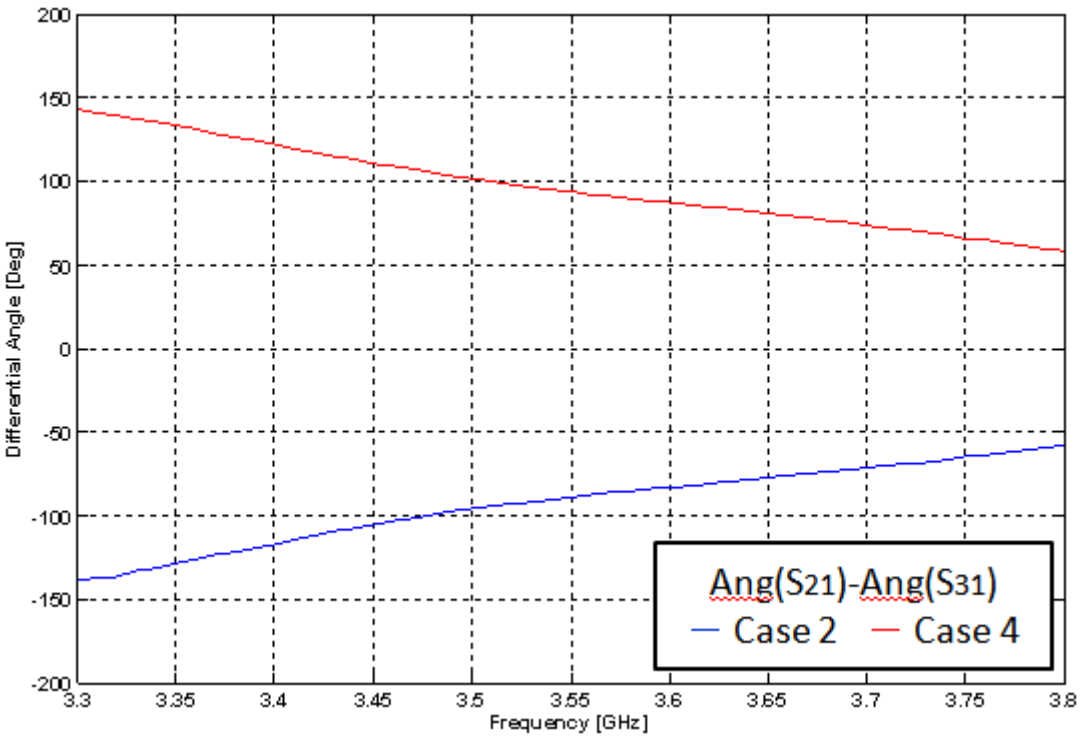

(b) WiMAX operation.

Figure 3-13 The measured angle difference of the dual-band BLC.

Chapter 4 Dual-band Patch Antenna

In this chapter, we will propose a square patch antenna fed by two L-shaped probe with four slots. The two L-shaped probes can effectively reduce the coupling effect between two ports. Moreover, the square patch with four slots can make the structure of the antenna symmetric and provide dual-band operation.

4.1 Antenna Design

The structure of slot is often adopted in the antenna design for either dual-band excitation or bandwidth enhancement. As shown in Fig. 4-1 [18], they propose a structure which consists of a rectangular patch loaded by two slots which are etched close to the radiating edges where the bandwidth is about 2% in two operating bands. In this structure, the slots are used to change the current of the TM_{30} mode on the rectangular patch and make the current distribution become more similar with the current distribution of TM_{10} and the current distribution in both operating band are shown in Fig. 4-2. However, because the patch is of the rectangular shape, it is hard to integrate two orthogonal linear polarization modes in a single patch. Moreover, two directly-fed coaxial probes in a single patch may cause serious coupling as well.

We therefore propose a square patch antenna fed by the L-shaped probe with four slots as shown in Fig. 4-3. The two slots along the X-direction are parallel to the X-direction current distribution on the square patch, so they will only disturb the X-direction current distribution slightly. Because it is a symmetric structure, we can therefore utilize two L-shaped probes feeding in orthogonal directions. This technique allows one square patch to set up two L-shaped probes along X and Y direction for producing two linear polarizations in a single patch and will not cause

serious coupling effect as well. The geometric size of AH, AG, Lp, Pw, SL, SG, Sw we implemented is 3mm, 0.5mm, 12.5mm, 47mm, 32.5mm, 2mm and 0.6mm respectively.

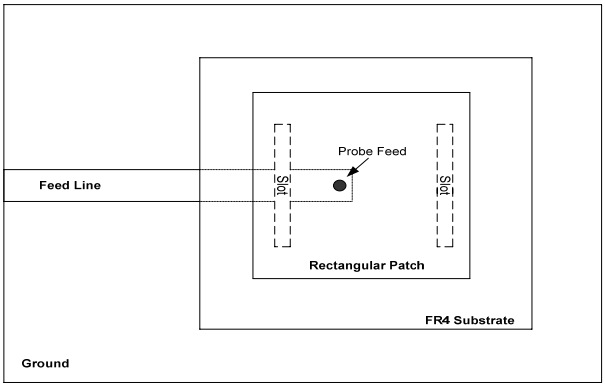

(a) Top view of probe-fed patch antenna with a pair of slots.

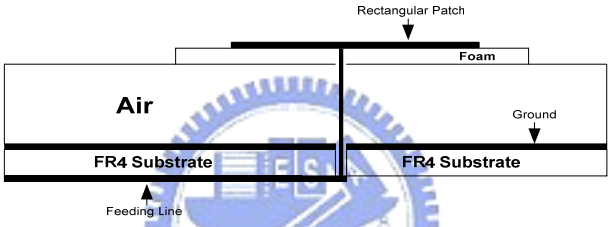

(b) Side view of probe-fed patch antenna with a pair of slots.

Figure 4-1 The probe-fed patch antenna with a pair of slots.

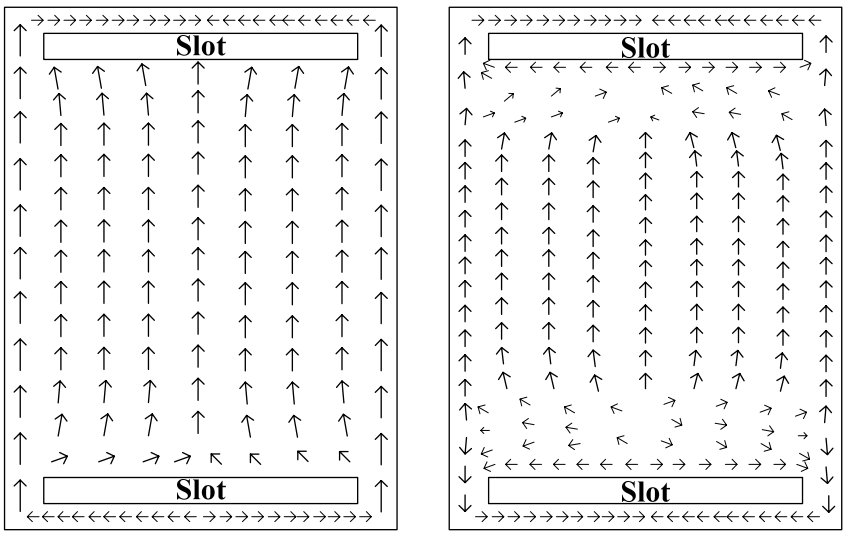

(a) (b)

Figure 4-2 The current distribution of the probe-fed patch antenna with a pair of slots. (a) Lower band (b) Higher band.

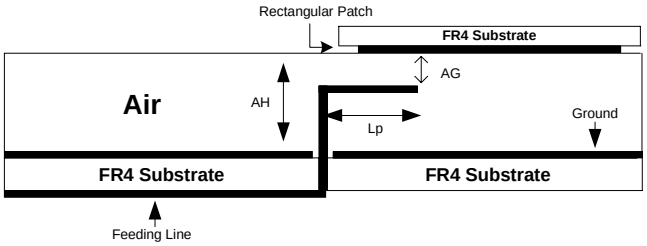

(a) Side view of L-shaped probe fed patch antenna

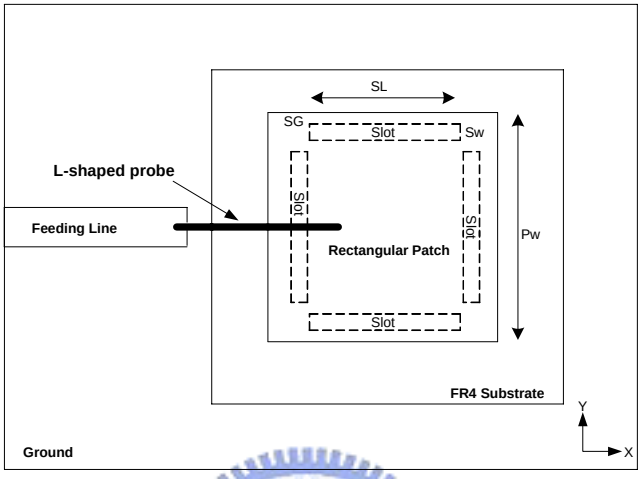

(b) Top view of L-shaped probe fed patch antenna with four slots

Figure 4-3 Patch antenna fed by L-shaped probe with four slots.

4.2 Simulation and Measurement Results

The simulation and measurement results are shown in Fig. 4-4. The performance of low S_{21} means coupling effect between two ports can be observed in both of the desired frequency bands. The simulated E-plane radiation pattern at 2.45GHz and 3.5GHz are shown in Fig. 4-5. Because the magnitude of cross-polarization pattern is lower -10 dB, it can be a good antenna candidate of linear polarization.

Fig. 4-6 shows the measured radiation patterns. The low cross polarization represents that the additional two X-direction slots only affect the X-direction current slightly. The measured bandwidth and maximum gain are 2.44 % and 9.23 dBi at 2.45GHz, respectively. On the other hand, the measured bandwidth and maximum

gain are 2.57 % and 8.7 dBi at 3.5GHz, respectively. The measured results are slightly different from the simulated results. It may be mainly because of the deviation of the size of the L-shaped probes and the gap between the L-shaped probe. The above reasons make the patch may not be fabricated in the symmetric manner.

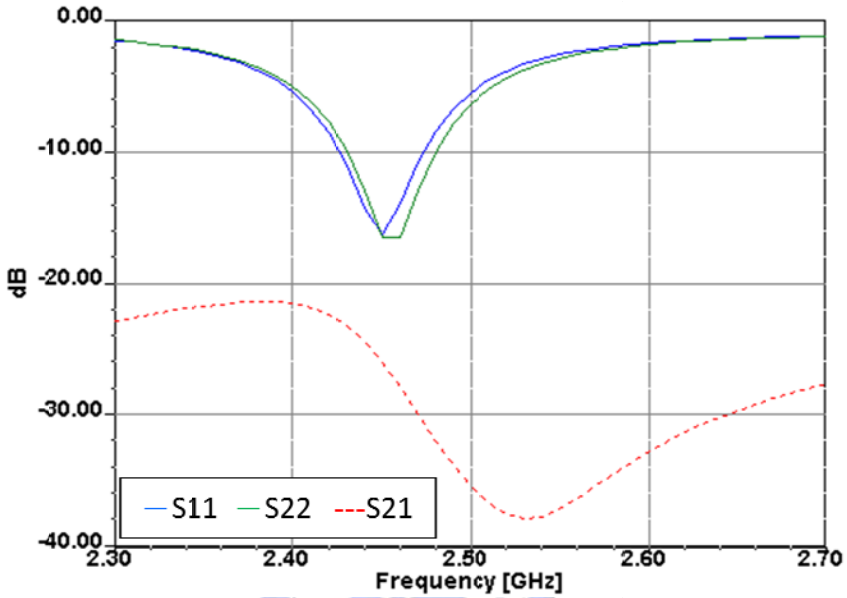

(a) The simulation result of the dual-band antenna in WiFi band.

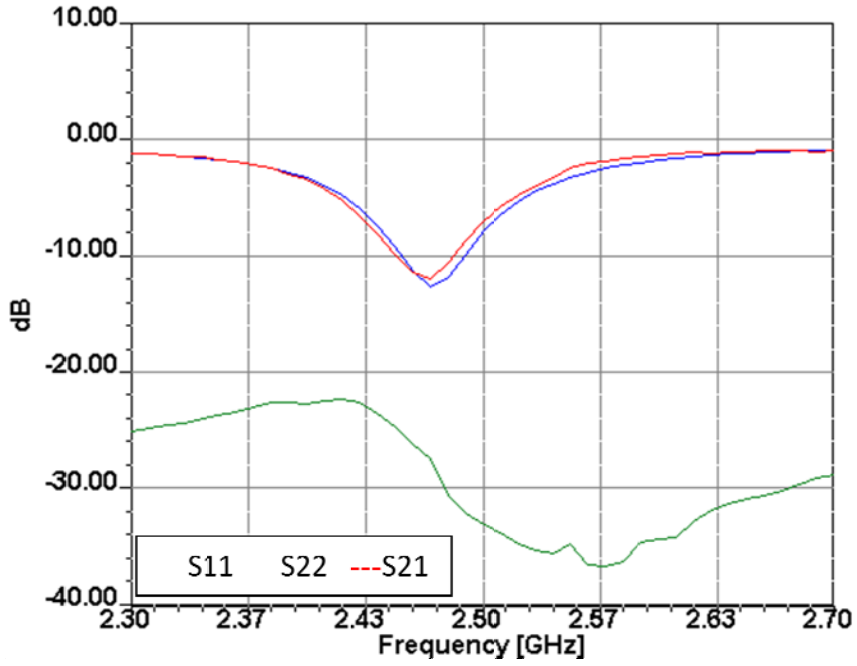

(b) The measured result of the dual-band antenna in WiFi band.

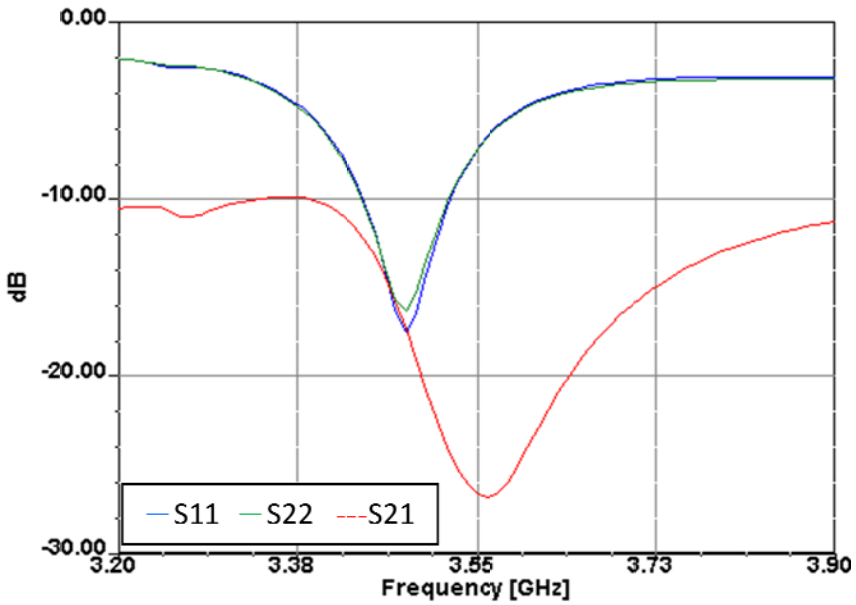

(c) The simulation result of the dual-band antenna in WiMAX band.

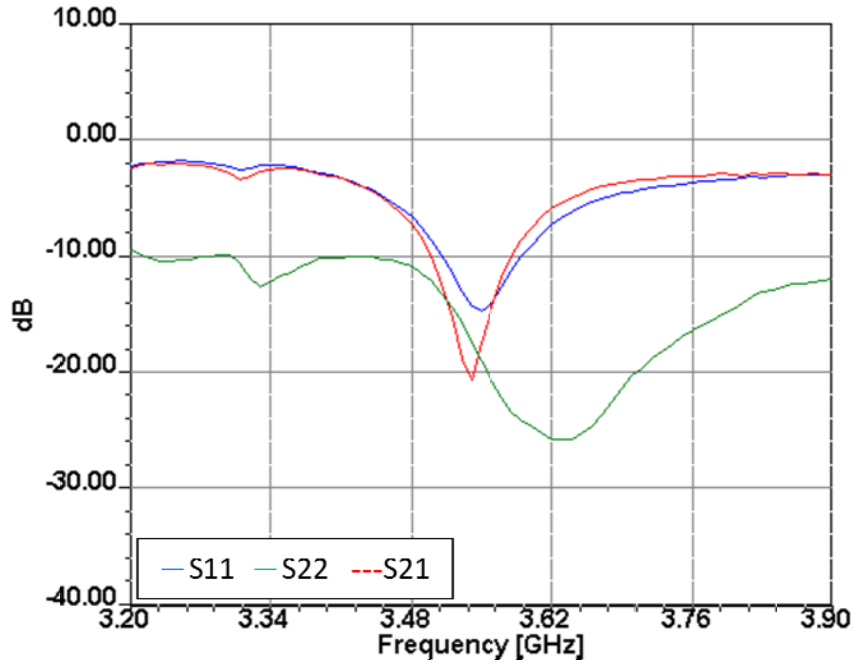

(d) The measured result of the dual-band antenna in WiMAX band.

Figure 4-4 The scattering parameters of the patch antenna with four slots fed by two orthogonal L-shaped probes.

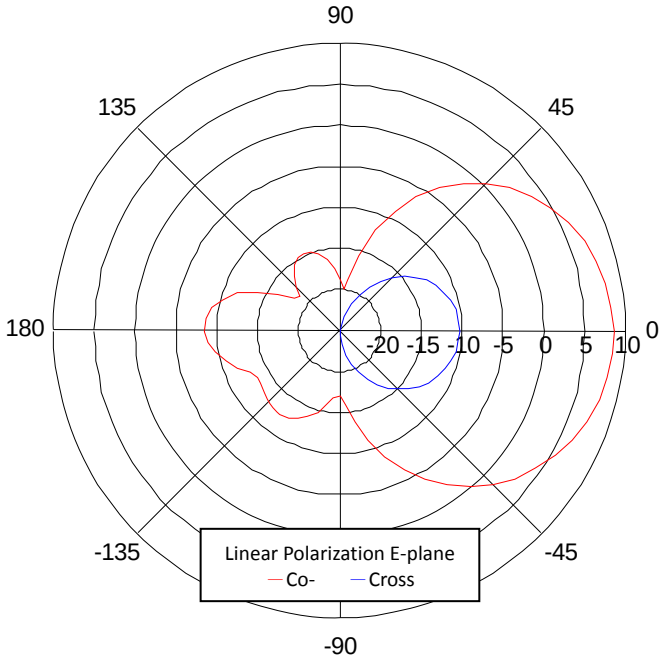

(a) The simulated E-plane radiation pattern at 2.45GHz.

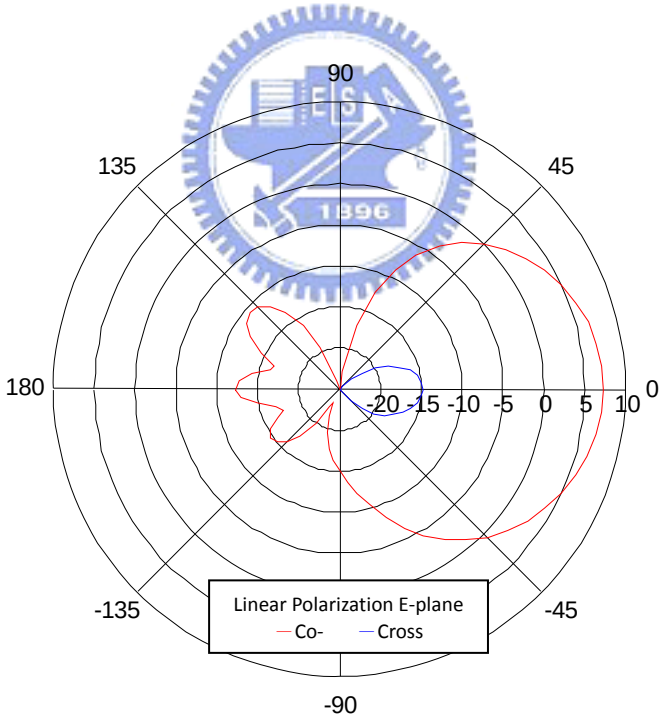

(b) The simulated E-plane radiation pattern at 3.5GHz.

Figure 4-5 The simulated patterns of the patch antenna with four slots fed by two orthogonal L-shaped probes.

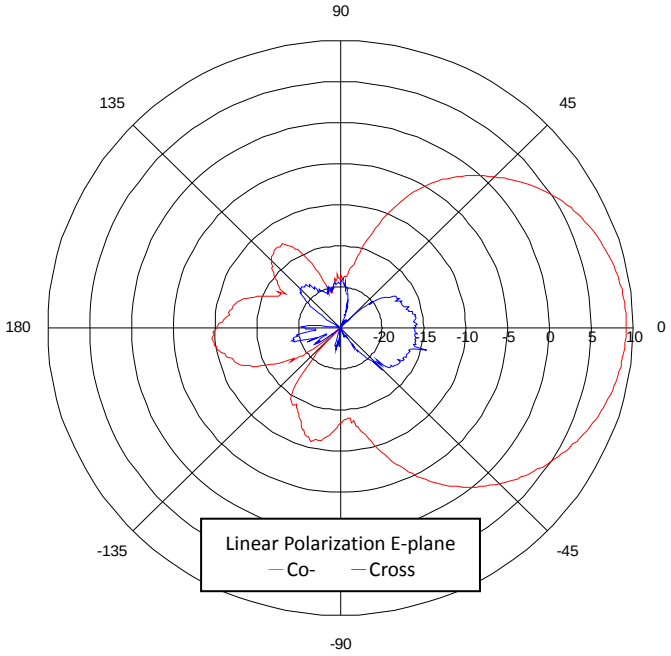

(a) The measured E-plane radiation pattern at 2.45GHz.

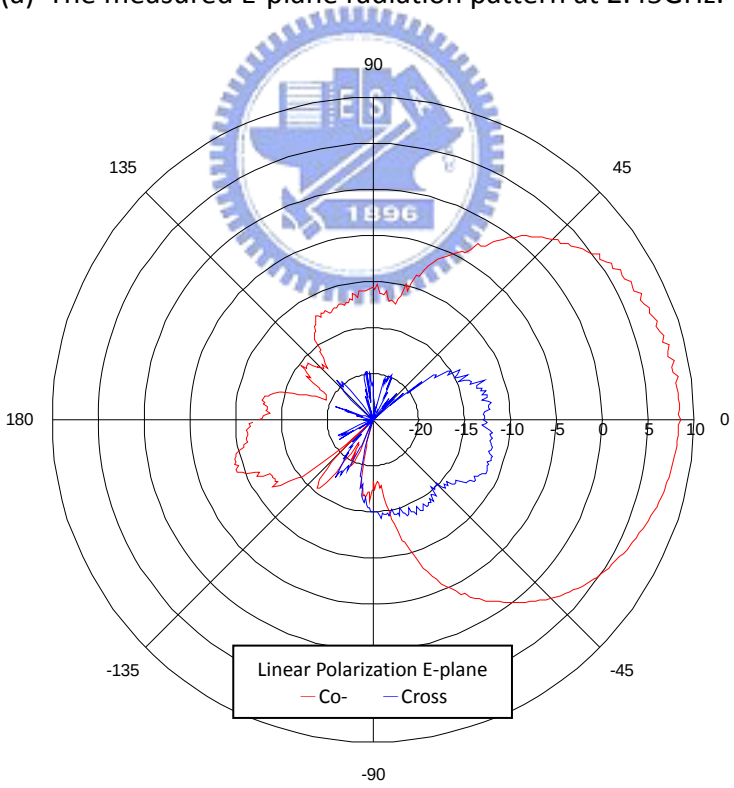

(b) The measured E-plane radiation pattern at 3.5GHz.

Figure 4-6 The measured patterns of the patch antenna with four slots fed by two orthogonal L-shaped probes.

Chapter 5 The Dual-band Reconfigurable Quadri-Polarization Diversity Antenna

We further combine the three parts (dual-band BLC, wideband switching circuit and dual-band patch antenna) which we have designed in the previous chapters and present its performances. The system block is shown in Fig. 5-1. As the wideband switching circuit 1 and switching circuit 2 operate at “Through” and “Termination” state respectively and the power is incident from port 1, the antenna can generate an X-directional linear polarization sense. As the wideband switching circuit 1 and switching circuit 2 both operate at “Through” state and the power is incident from port 1, the antenna can generate a left-hand circular polarization sense in WiFi operation. In the same manner where the power is incidence from port4, the antenna can generate a right-hand circular polarization sense in WiFi operation. The operating modes of the proposed antenna are shown in Table 5-1. From Table 5-1, we find as the wideband switching circuits change their states, the antenna structure can provide quadri-polarization in both operating bands.

5.1 Simulation and Measurement Results

The top view of the whole simulated antenna structure in HFSS is shown in Fig. 5-2. The simulated scattering parameters in Case 1 (port 1 excitation) and Case 3 (port 2 excitation) state are shown in Fig. 5-3, and simulated scattering parameters of Case 2 (port 1 excitation) and Case 4 (port 4 excitation) state are shown in Fig. 5-4. From the simulated scattering parameters we know the whole antenna structure is feasible for covering each of the required bandwidth. The simulated radiation patterns of Case 1 are shown in Fig. 5-5. The simulated maximum gain in case 1 state

is 2.7dBi in WiFi and 2.2dBi in WiMAX operation, respectively. From the simulation results, since the cross-polarization pattern is very small compared to the co-polarization pattern, the antenna is convinced to have good operation in either linear polarization or circular polarization.

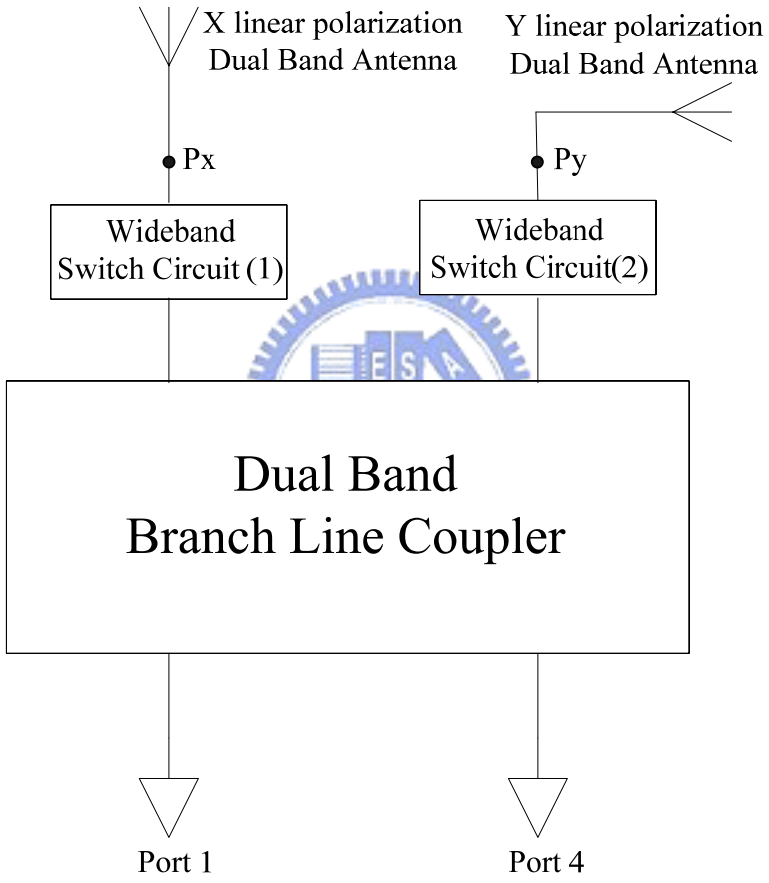

Figure 5-1 The system block of the dual-band antenna structure.

Table 5-1 STATUTES OF THE DUAL-BAND ANTENNA STRUCTURE.

	Input	Switching circuit (1)	Switching circuit (2)	Polarization sense
Case 1	**Port 1**	**Through**	**Termination**	**X-direction Linear Polarization**
Case 2	**Port 1**	**Through**	**Through**	**LHCP (WiFi operation) RHCP (WiAX operation)**
Case 3	**Port 4**	**Termination**	**Through**	**Y-direction Linear Polarization**
Case 4	**Port 4**	**Through**	**Through**	**RHCP (WiFi operation) LHCP (WiAX operation)**

The photograph of the antenna structure is shown in Fig. 5-6. The measured performances of scattering parameters are shown in Fig. 5-7 and Fig. 5-8, and the bandwidth is 5.7% and 6% in WiFi and WiMAX operation respectively. The measured radiation patterns are shown in Fig. 5-9 to Fig. 5-13. In Fig. 5-9 and Fig. 5-10, since the cross-polarization pattern is very small compared to the co-polarization pattern, the dual-band antenna is good for operating in linear polarization. In Fig. 5-11a, the maximum gain is 2.5dBi and the 2-dB axial-ratio beamwidth is 86° at 2.45GHz in Case 2. In Fig. 5-11b, we can observe the maximum gain is about 1.9dBi and the 2-dB axial-ratio beamwidth is 78° at 3.5GHz in Case 2. The measured performances of the dual-band structure are listed in Table 5-2. In Table5-2, the quadri-polarization beamwidth means the axial-ratio of LHCP and RHCP are lower than 2dB and the magnitude of cross polarization of LP in Case 1 and Case 3 are lower than -10dB in this beamwidth in each operating band.

The measured maximum gain of Case 2 is little larger than the measured maximum gain of Case 4 by 0.3dBi in 2.45GHz and 0.24dBi in 3.5GHz, as shown in Table 5-2. To explain this phenomenon, we must survey the power actually radiated

by the dual-band patch antenna. Therefore, we have to get the scattering parameters of the dual-band patch antenna and dual-band BLC individually. In Section 3-3, we have got the simulated and measured scattering parameters of S_{21} and S_{31}, which can be considered A_1 and A_2 respectively, the power incident to two L-shaped probes of the dual-band patch antenna. In Section 4-2, we had simulated and measured scattering parameters of the dual-band patch antenna, which can be considered a set of S_{ANT}. And the reflected power at P_x and P_y in Fig. 5-1 can be obtained by the following equation

$$\begin{bmatrix} b_1 \\ b_2 \end{bmatrix} = [S_{ANT}] \cdot \begin{bmatrix} A_1 \\ A_2 \end{bmatrix} = \begin{bmatrix} S_{11} & S_{21} \\ S_{12} & S_{22} \end{bmatrix} \cdot \begin{bmatrix} A_1 \\ A_2 \end{bmatrix} \tag{5-1}$$

where b_1 and b_2 is the quantity of reflected power at P_x and P_y respectively. Therefore, the normalized power actually radiated by the dual-band patch antenna is

$$\overline{P}_{ANTi} = \frac{P_{ANTi}}{P_i} = |A_1|^2 + |A_2|^2 - |b_1|^2 - |b_2|^2 \tag{5-2}$$

where the P_i is the input power at port 1 or port 4 and the P_{ANTi} is the power actually radiated by the dual-band patch antenna. We first discuss the simulated results of P_{ANTi}. In simulated results we get the parameters of A1, A2 and S_{ANT} and substitute them into Equation (5-2). We can therefore obtain b_1 and b_2, and the normalized power ($\overline{P}_{ANTi}$) actually radiated by the dual-band patch antenna is 0.686 and 0.685 in Case 2 and Case 4 state respectively in 2.45GHz. In the same manner, we can get the normalized power ($\overline{P}_{ANTi}$) actually radiated by the dual-band patch antenna is 0.554 and 0.548 in Case 2 and Case 4 state respectively in 3.5GHz. From the computation results in both frequency bands, because 1) the antenna structure is symmetric, 2) the lumped elements in HFSS are lossless and 3) the values of lumped element don't vary with frequency, the power radiated by the dual-band patch antenna is almost equal in both of the two circular polarization states.

Different from the simulated ones, the measured A1, A2 and SANT can be gotten from the previous chapter 3 and chapter 4 and we can use the same analysis sequence to find the solutions of $\overline{P}_{ANTi}$. The normalized power ($\overline{P}_{ANTi}$) actually radiated by the dual-band patch antenna is 0.508 and 0.403 in Case 2 and Case 4 state respectively in 2.45GHz, and the normalized power ($\overline{P}_{ANTi}$) actually radiated by the dual-band patch antenna is 0.462 and 0.448 in Case 2 and Case 4 state respectively in 3.5GHz. Obviously, the measured result $\overline{P}_{ANTi}$ is lower than the simulated result of $\overline{P}_{ANTi}$, and it's caused by the practical lumped elements provide extra power loss. Moreover, the measured result of $\overline{P}_{ANTi}$ in Case 4 is lower than the measured result of $\overline{P}_{ANTi}$ in Case 2. The calculated difference between Case 2 and Case 4 is 0.06 in 2.45GHz and 0.08 in 3.5GHz, so the measured maximum gain in Fig. 5-11 is slightly larger than the measured maximum gain in Fig. 5-12 by 0.22dBi in 2.45GHz and 0.24dBi in 3.5GHz. The main reason of the imbalance may be that A1 and A2 of Case 2 is a little different from those of Case 4 at both frequency bands, so the actual radiated power of Case 2 and Case 4 will not be the same and result in the asymmetric pattern gain at both frequency bands.

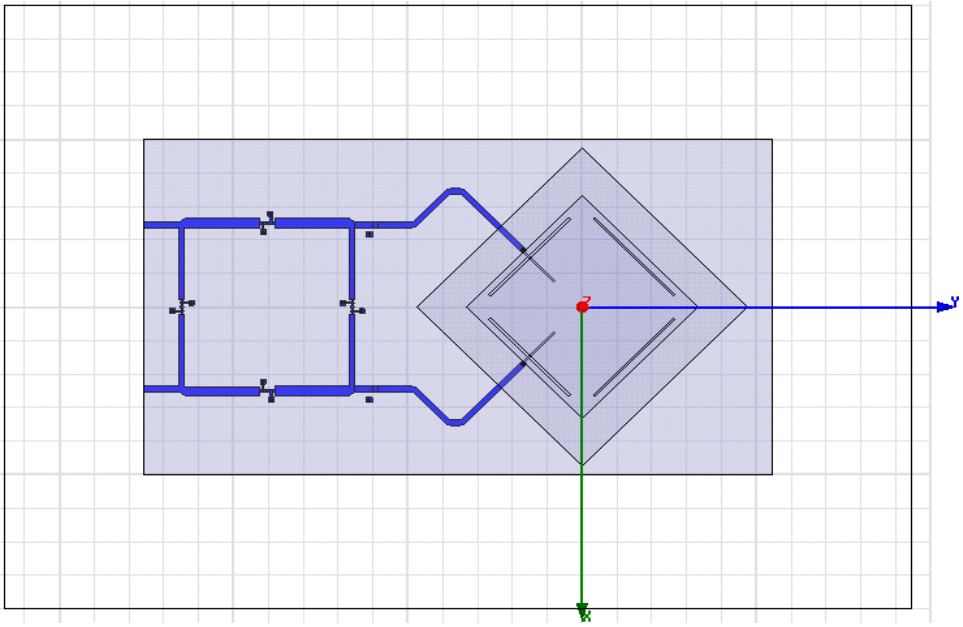

Figure 5-2 The top view of simulated antenna structure in HFSS.

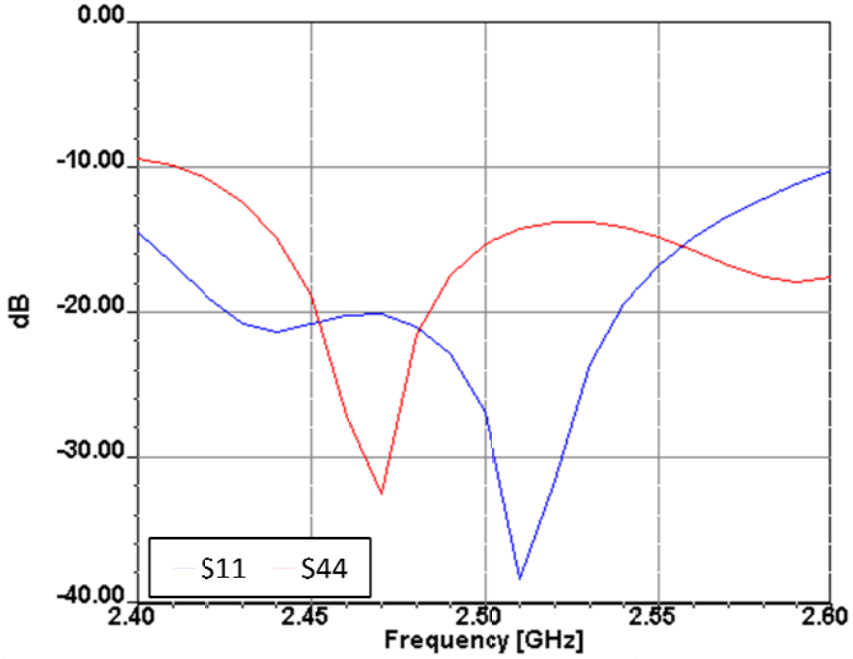

(a) WiFi operation.

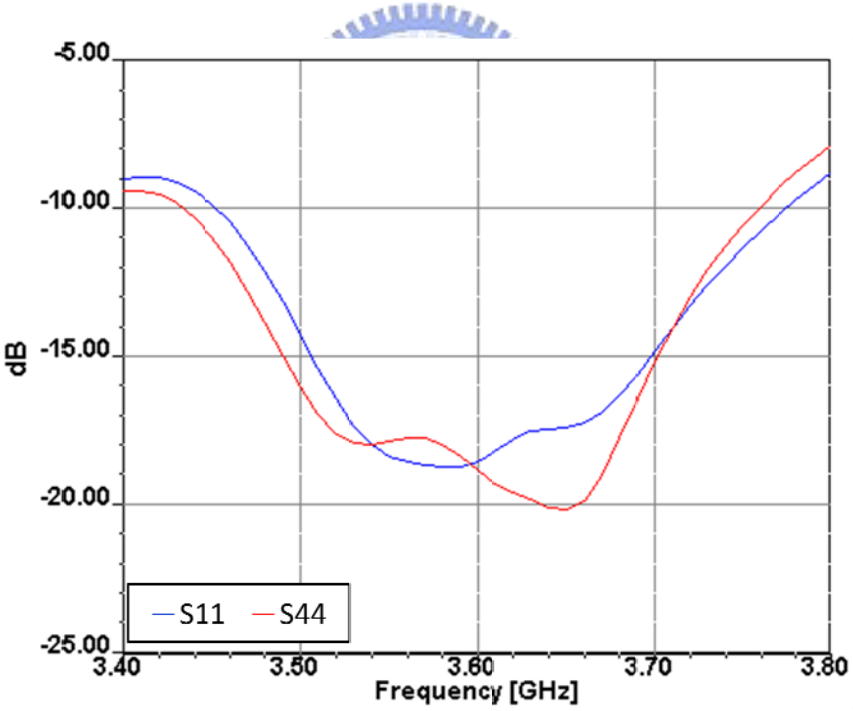

(b) WiMAX operation.

Figure 5-3 The simulated scattering parameters in Case 1 and Case 3 state.

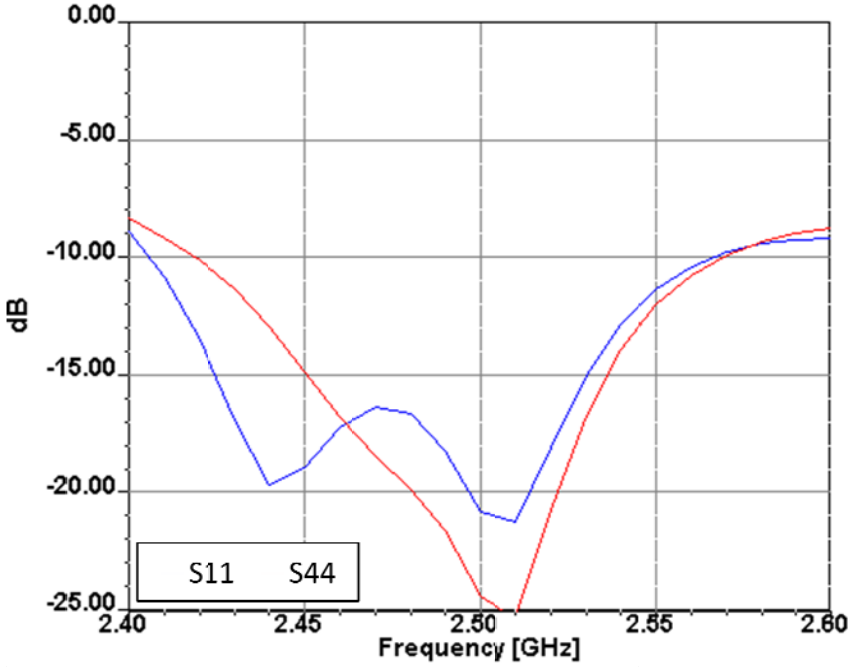

(a) WiFi operation.

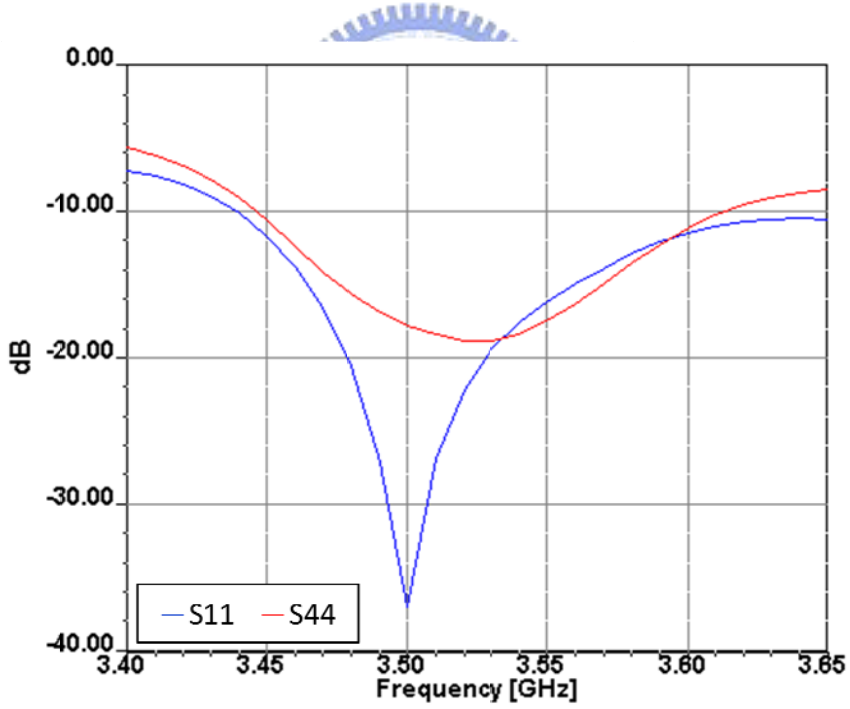

(b) WiMAX operation.

Figure 5-4 The simulated scattering parameters in Case 2 and Case 4 state.

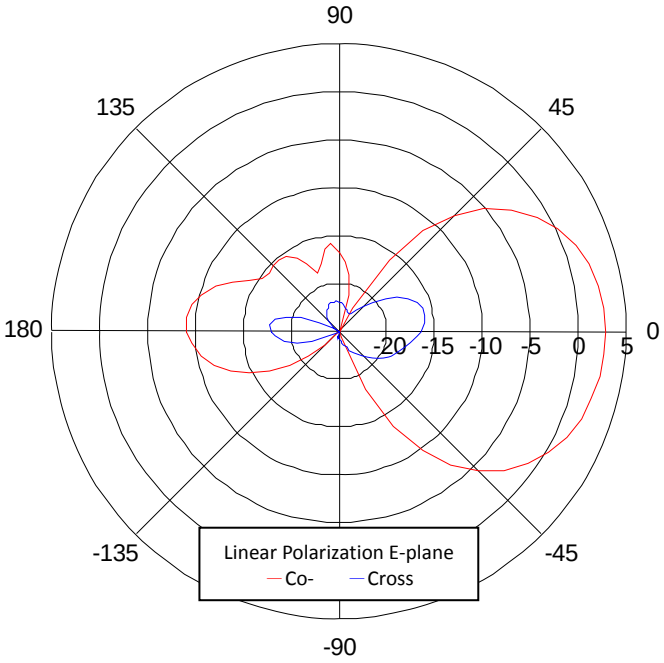

(a) 2.45GHz.

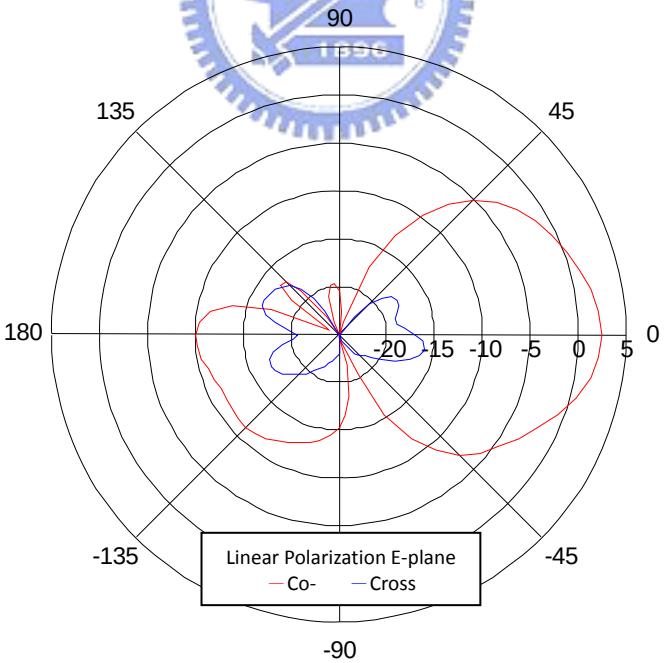

(b) 3.5GHz

Figure 5-5 The simulated radiation patterns in Case 1.

(a) (b)

Figure 5-6 The photographs of the dual-band quadri-polarization diversity patch antenna. (a) Front side of the structure. (b) Back side of the structure.

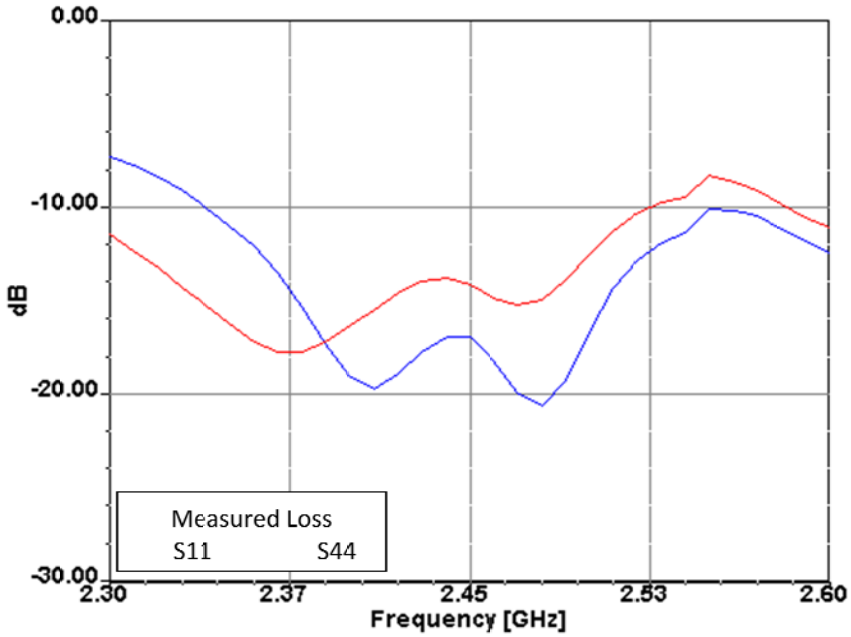

(a) WiFi operation.

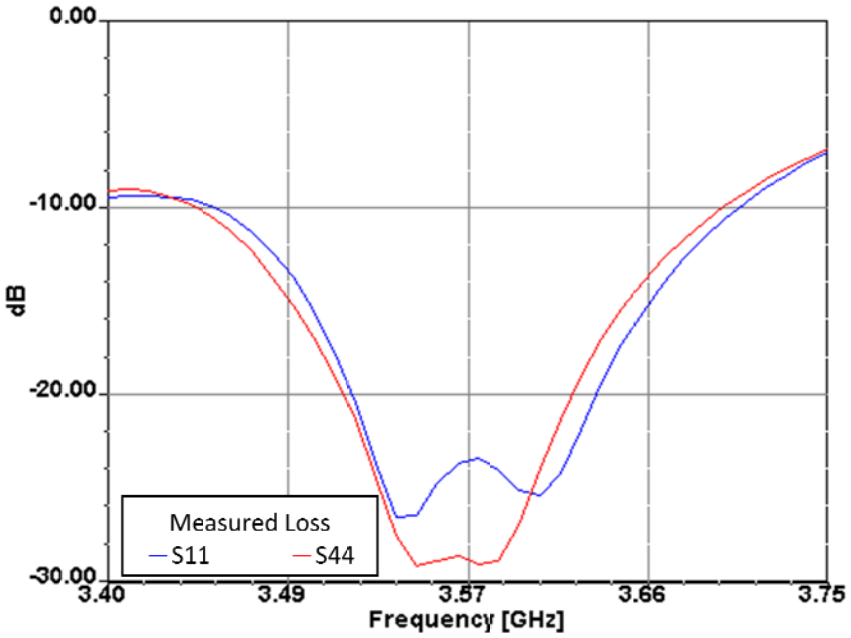

(b) WiMAX operation.

Figure 5-7 The measured scattering parameters of the antenna structure for Case 1 and Case 3.

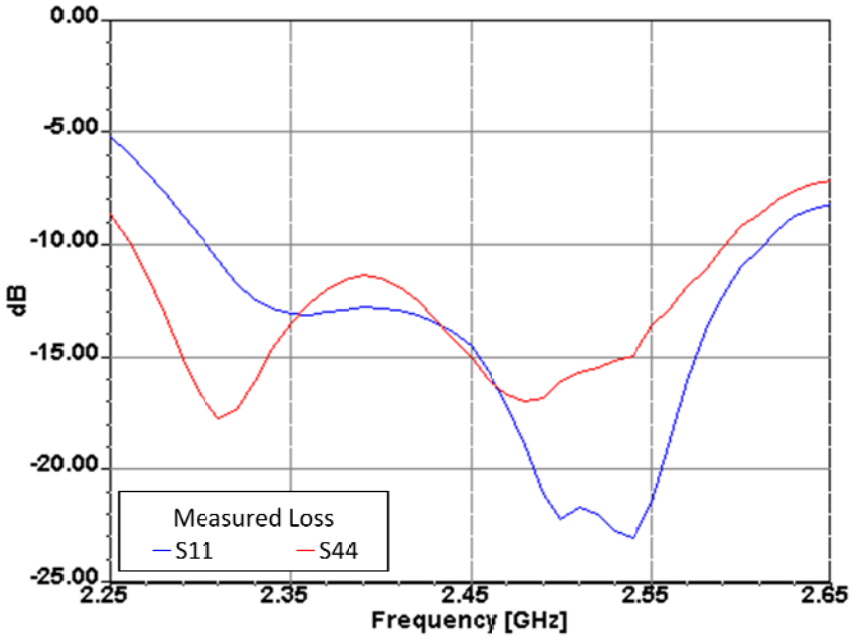

(a) WiFi operation.

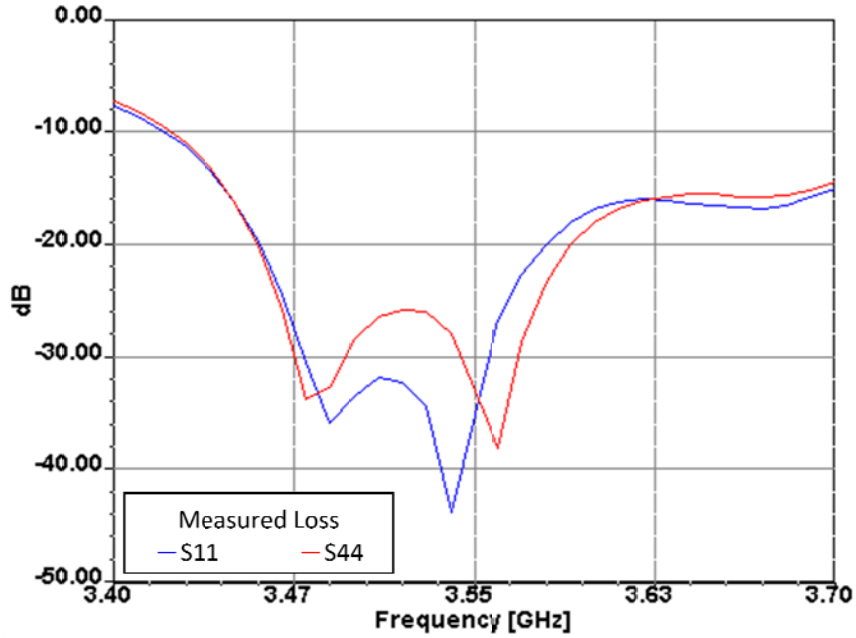

(b) WiMAX operation.

Figure 5-8 The measured scattering parameters of the antenna structure for Case 2 and Case 4.

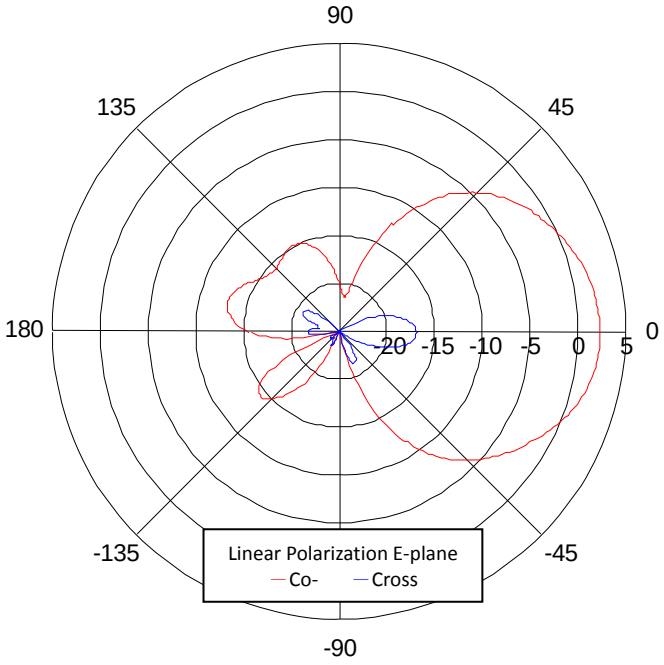

(a) The measured E-plane radiation pattern at 2.45GHz.

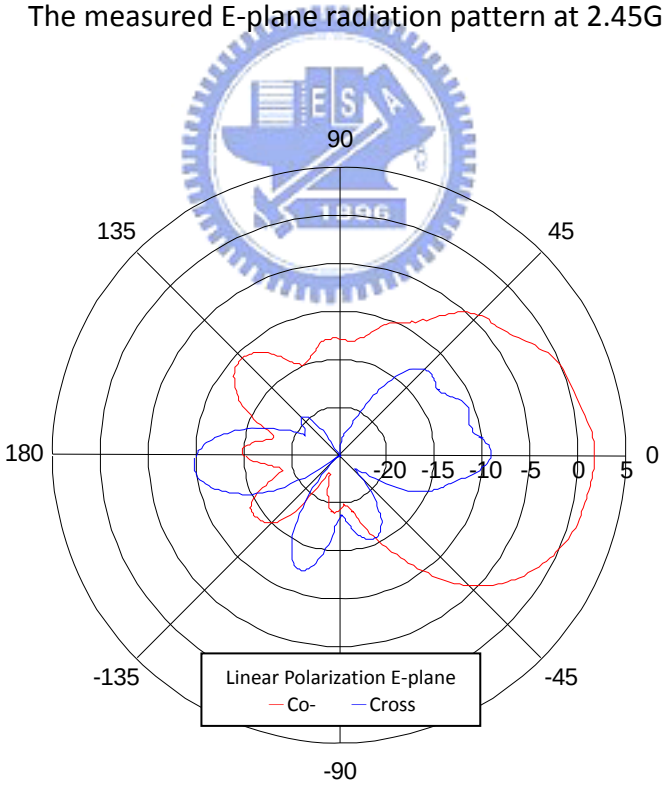

(b) The measured E-plane radiation pattern at 3.5GHz.

Figure 5-9 The measured E-plane radiation patterns in Case 1 state.

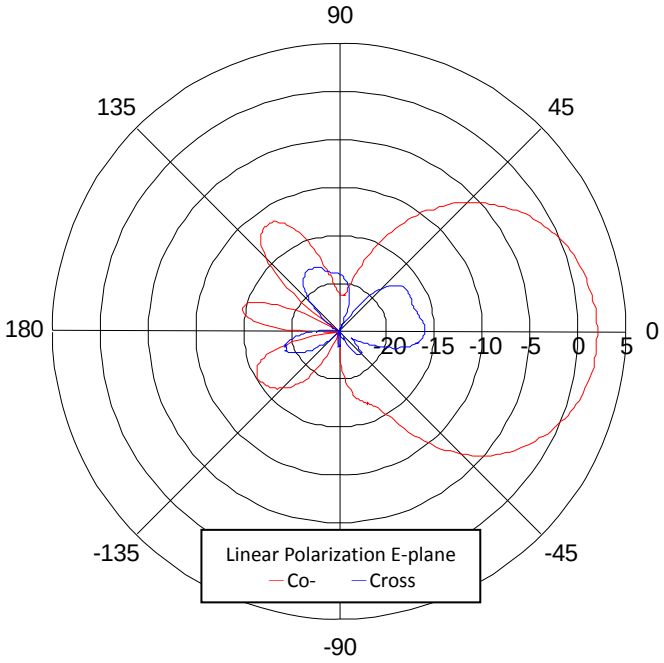

(a) The measured E-plane radiation pattern at 2.45GHz.

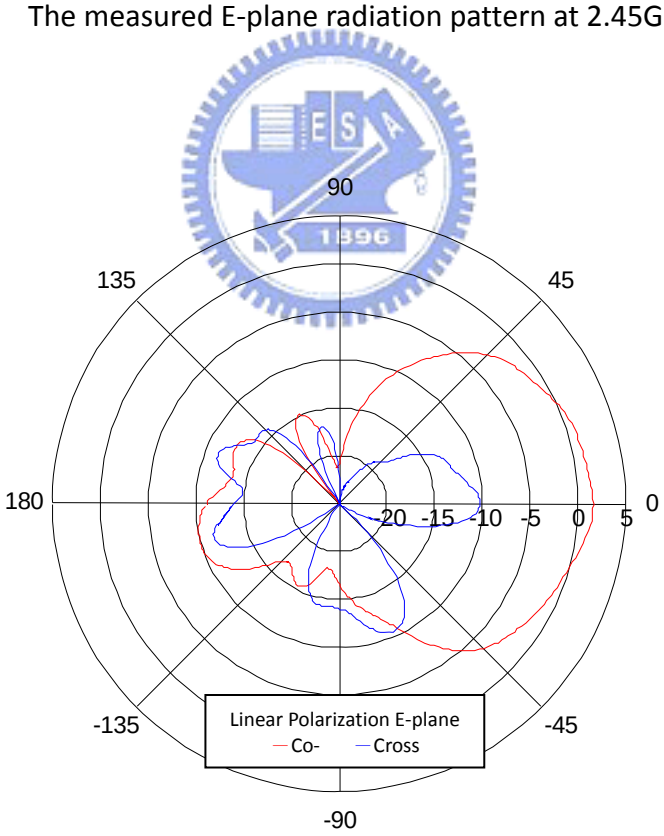

(b) The measured E-plane radiation pattern at 3.5GHz.

Figure 5-10 The measured E-plane radiation patterns in Case 3 state.

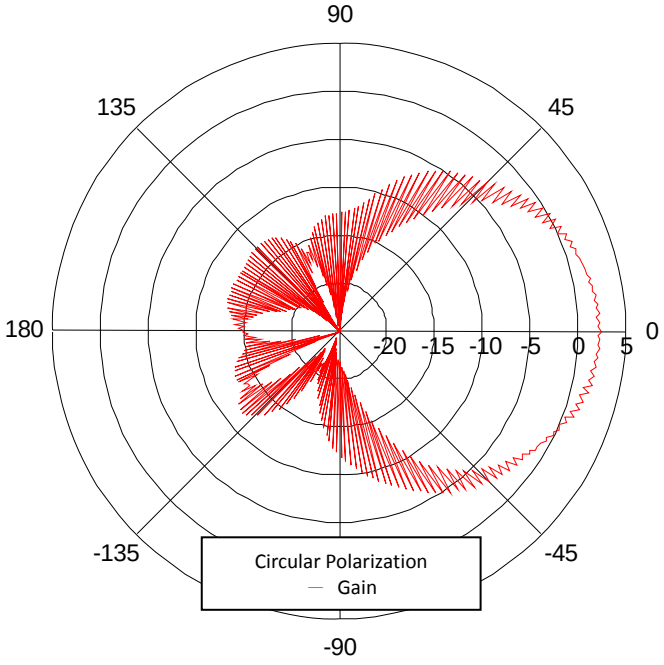

(a) Measured circular polarization radiation pattern at 2.45GHz.

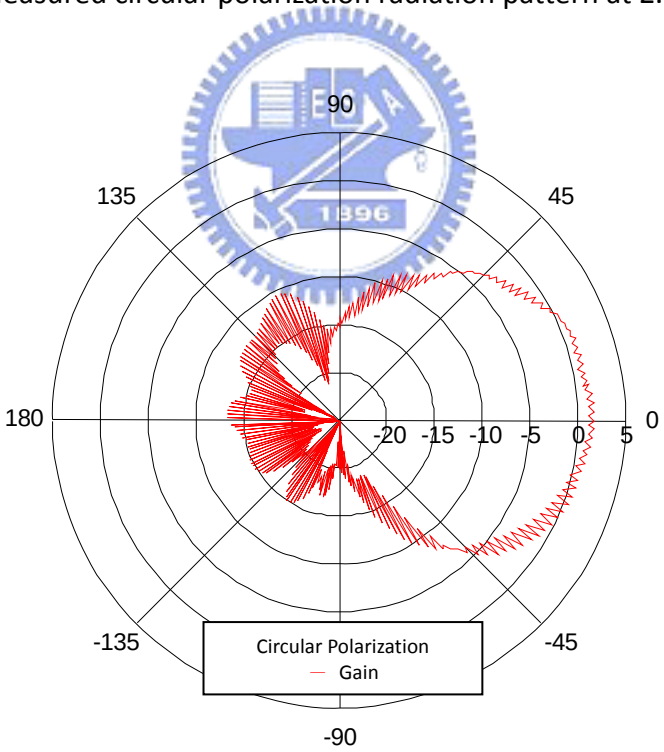

(b) Measured circular polarization radiation pattern at 3.5GHz

Figure 5-11 The measured radiation patterns in Case 2 state.

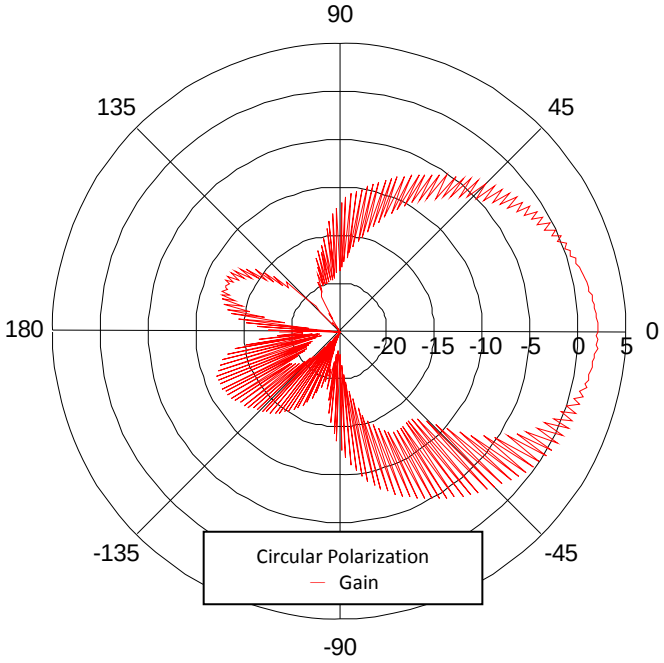

(a) Measured circular polarization radiation pattern at 2.45GHz.

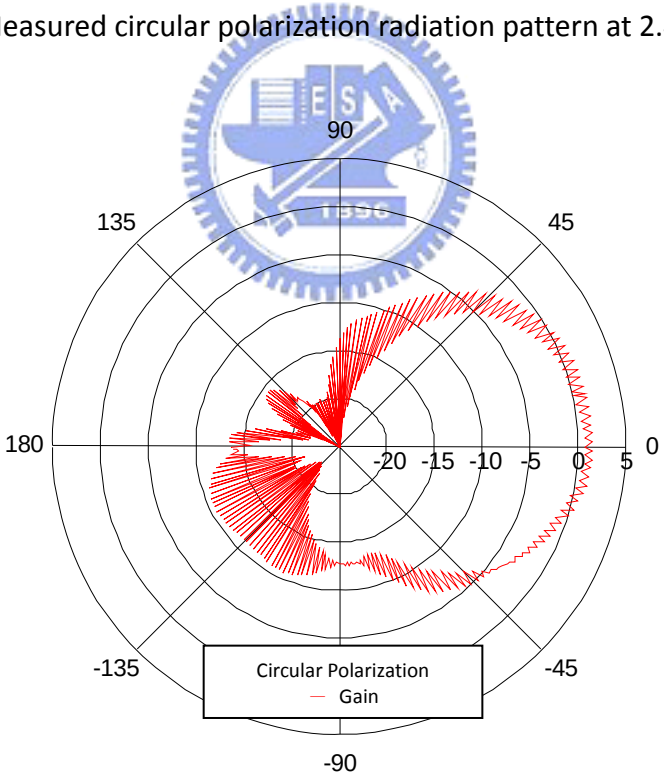

(b) Measured circular polarization radiation pattern at 3.5GHz.

Figure 5-12 The measured radiation patterns in Case 4 state.

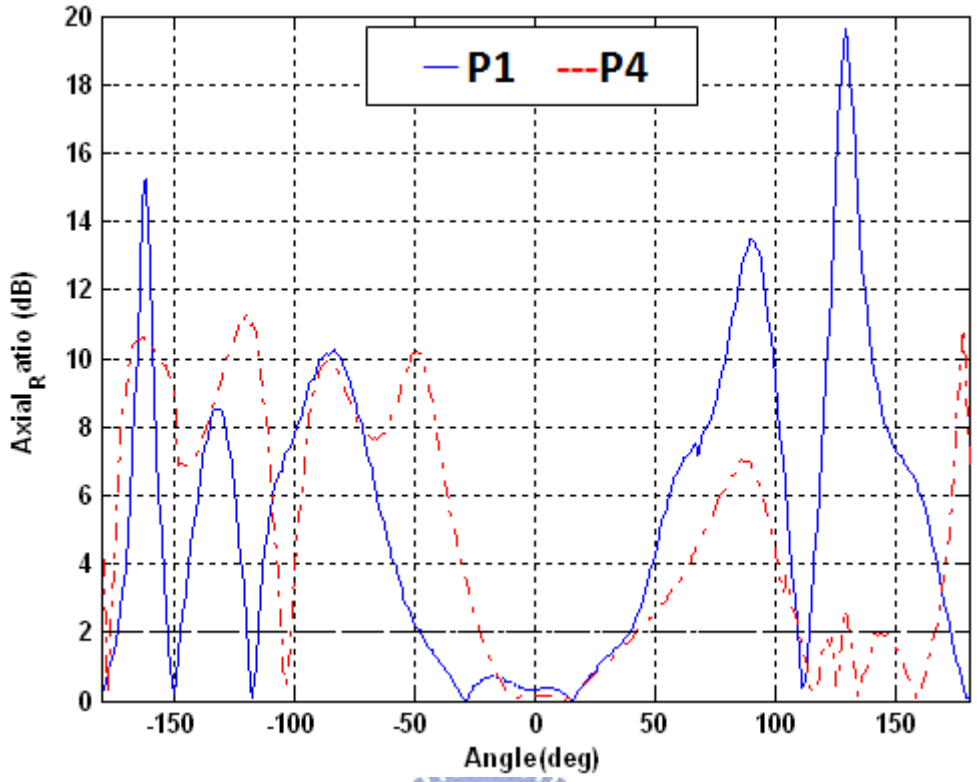

(a) 2.45GHz.

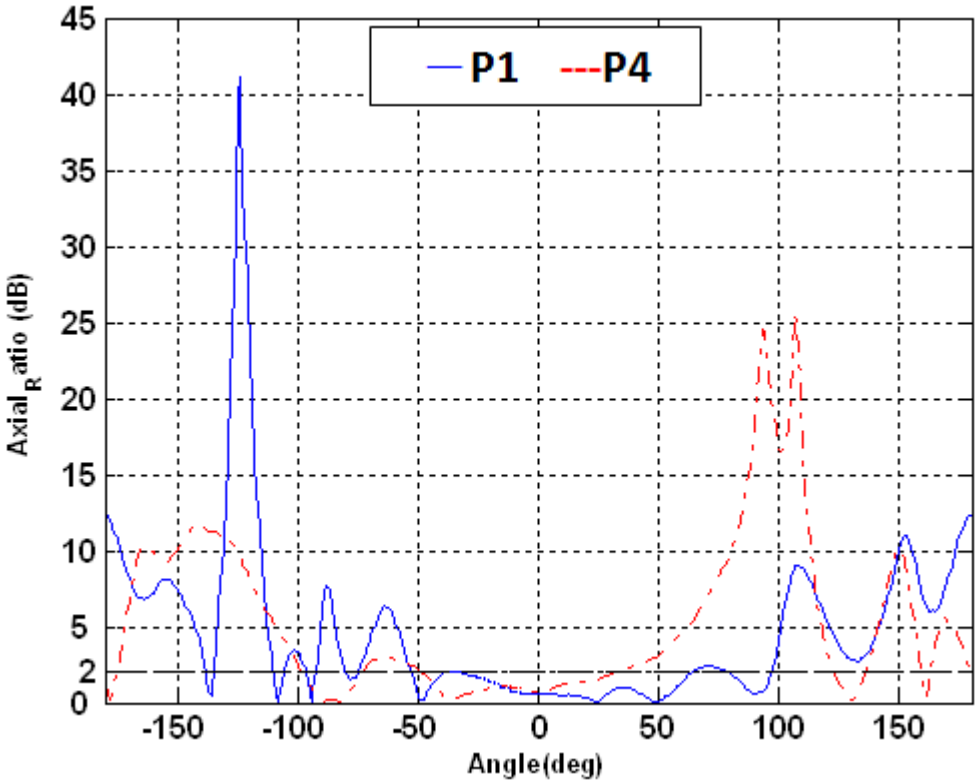

(b) 3.5GHz.

Figure 5-13 The measured axial-ratio of the proposed antenna.

Table 5-2 THE MEASURED PERFORMANCES OF THE DUAL-BAND ANTENNA STRUCTURE.

Frequency	Polarization Sense	Axial Ratio < 2 Beamwidth (Deg)	Quadri-Polarization Beamwidth (Deg)	Maxinum Gain (dBi)
2.45GHz	RHCP (Case 4)	65	65	2.18
	LHCP (Case 2)	90		2.4
	LP (Case 1)	XXX		2.3
	LP (Case 3)	XXX		2
3.5GHz	RHCP (Case 2)	95	70	1.8
	LHCP (Case 4)	80		1.56
	LP (Case 1)	XXX		1.76
	LP (Case 3)	XXX		1.63

Chapter 6 Conclusion

We have provided another even-odd mode method to design the dual-band BLC and combined it with the wideband switching circuits successfully in Chapter 3. With the wideband switching circuit, we can easily control the power to either go through the circuit or be absorbed by 50-Ohm termination from 2 GHz to 6 GHz. The dual-band BLC provides two equal power signals with 90° phase difference in two operating bands. In Chapter 4, a dual-band patch antenna with low cross polarization and coupling has been completely fabricated. Because of the symmetry of the antenna structure we proposed, two L-shaped probes can be easily integrated in a single patch, and the four additional slots are etched close to each radiation side to produce another radiation frequency. Finally, we combine the above three parts to fabricate a single patch antenna structure with dual-band reconfigurable quadri-polarization diversity. The measured results in Chapter 5 have shown our proposed dual-band quadric-polarization diversity antenna meets our expectation.

WiFi and WiMAX systems are becoming more popular in wireless communication applications. And one antenna structure operating in these two bands is becoming more important. Our antenna design can be one of the best solutions for enhancing the communication quality. The idea we present in this thesis is good but there is still room for improvement to reach better performance. First, we may design a better switching circuit to increase the antenna gain and reduce the lump elements. Moreover, the design of the dual-band quadri-polarization diversity antenna is convinced a rising topic and we provide one as a milestone for this demand. We believe the design of dual-band quadri-polarization diversity antenna will greatly bring contribution to the communication technology.

References

[1] 吳逸凡，「新型可塑性四極化天線設計」，國立交通大學，碩士論文，民國94年。

[2] 吳俊賢，「可塑性四極化掃描天線之設計」，國立交通大學，碩士論文，民國95年。

[3] W. L. Stutzman and G. A. Thiele, *Antenna Theory and Design*, 2nd ed. New York: Wiley, p. 212-215, 1998.

[4] C. L. Mak, K. M. Luk, K. F. Lee and Y. L. Chow, "Experimental Study of a Microstrip Patch Antenna with an L-shaped Probe", *IEEE Trans. Antenna & Propagation*, vol. 48, pp.777-783, May 2000.

[5] I-Hsiang Lin, Marc DeVincentis, Christophe Caloz and Tatsuo Itoh, "Arbitrary Dual-Band Components Using Composite Right/Left -Handed Transmission Lines", *IEEE Trans. Microwave Theory and Techniques*, vol. 52, pp. 1142-1149, Apr. 2004.

[6] K. R. Carver and J. W. Mink, "Microstrip Antenna Technology", *IEEE Trans. Antenna & Propagation*, vol. AP-29, pp. 2-24, Jan. 1981.

[7] D. H. Schaubert, "Microstrip Antenna", *Electromagnetics*, vol. 12, pp. 381-401, July- December 1992.

[8] R. E. Munson, "Conformal Microstrip Antennas and Microstrip Phased Arrays", *IEEE Trans. Antennas & Propagation*, vol. AP-22, pp.74-78, Jan. 1974.

[9] D. R. Jackson and N. G. Alexopoulos, "Simple Approximate Formulas for Input Resistance, Bandwidth, and Efficiency of a Resonant Rectangular Patch", *IEEE Trans. Antennas & Propagation*, vol. 3, pp.407-410, Mar. 1991.

[10] R. Q. Lee, K. F. Lee and J. Bobinchak, "Characteristics of a two-layer electromagnetically coupled rectangular patch antenna", *Electron. Lett.*, vol. 23, pp. 1070–1072, Sep. 1987.

[11] E. Chang, S. A. Long and W. F. Richards, “Experimental investigation of electrically thick rectangular microstrip antennas”, *IEEE Trans. Antennas & Propagation*, vol. AP-43, pp. 767–772, Jun. 1986.

[12] T. M. Au, K. F. Tong and K. M. Luk, “Characteristics of aperture-coupled co-planar microstrip subarrays”, *Inst. Elect. Eng. Proc. Microwave Antennas Propagat.*, vol. 144, pp. 137–140, Apr. 1997.

[13] K. M. Luk, C. L. Mak, Y. L. Chow and K. F. Lee, “Broadband microstrip patch antenna”, *Electron. Lett.*, vol. 34, pp. 1442–1443, Jul. 1998.

[14] H. Nakano, M. Yamazaki and J. Yamauchi, “Electromagnetically coupled curl antenna”, *Electron. Lett.*, vol. 33, pp. 1003–1004, Jun. 1997.

[15] H. Nakano, M. Yamazaki and J. Yamauchi, “Electromagnetically coupled curl antenna”, *Electron. Lett.*, vol. 33, pp. 1003–1004, Jun. 1997.

[16] David M. Pozar and Sean M. Duffy, “A Dual-Band Circular Polarized Aperture-Coupled Stacked Microstrip Antenna for Global Positioning Satellite”, *IEEE Trans. Antennas & Propagation*, vol. 45, pp. 1618-1625, Nov. 1997.

[17] Stephen D. Targonski and David M. Pozar, “Design of Wideband Circular Polarized Aperture-Coupled Microstrip Antennas”, *IEEE Trans. Antennas & Propagation*, vol. 41, pp. 214-219, Feb. 1993.

[18] S. Maci, G. B. Gentili and G. Avitabile, “Single-layer dual frequency patch antenna”, *Electron. Lett.,* vol. 29, pp. 1441-1443, Aug. 1993.